Acta Geochim (2025) 44:1167–1185
https://doi.org/10.1007/s11631-025-00833-3

ORIGINAL ARTICLE

Critical processes controlling the formation of visible gold in the giant Jiaodong gold province: Constraints from microtextural and geochemical analyses by SEM, TOF–SIMS, and LA-(MC)-ICP-MS

Hong Wang[1] · Ting-Guang Lan[1] · Lang-Ye Zhao[1,2] · Hong-Rui Fan[3] · Zhan-Ping Li[4] · Huan-Long Hu[1] · Zi-Qi Xu[3] · Hong-Wei Peng[1] · Lei Shu[5]

Received: 30 June 2025 / Revised: 27 September 2025 / Accepted: 9 October 2025 / Published online: 1 November 2025

Abstract The world-class Jiaodong gold province in the North China Craton hosts over 5000 t of Au resource and is characterized by abundant visible gold mineralization. However, the critical processes controlling the formation of visible gold in this province remain poorly understood. To solve this problem, integrated microtextural, trace elemental, and sulfur isotopic analyses of pyrite from the high-grade Linglong gold deposit in the Jiaodong gold province were conducted in this study. Two distinct pyrite types were identified within auriferous quartz-sulfide veins: (1) Py1 aggregates in quartz-pyrite veins (hydrothermal stage II), and (2) euhedral to subhedral, coarse-grained Py2 crystals in quartz-polymetallic sulfide veins (hydrothermal stage III). Microtextural and elemental analyses revealed that visible gold predominantly occurs as intergranular particles between primary pyrite crystals within Py1 aggregates. The Py1 exhibits complex microtextures with abundant mineral inclusions of polymetallic sulfides and has low concentrations of Au (median: 0.032 ppm) with a narrow δ^{34}S range (4.86‰–6.75‰), indicative of rapid crystallization under unstable, disequilibrium conditions. By contrast, the Py2 is texturally homogeneous and contains higher Au concentrations (median: 0.304 ppm) with progressively increasing δ^{34}S values (5.25‰–10.14‰) over time, suggesting slow crystal growth under more stable, near-equilibrium conditions. Based on the microtextural and geochemical information, it is proposed that fluid boiling occurred only during the hydrothermal stage II, which resulted in the unstable physicochemical environment and rapid deposition of gold. During the boiling processes, gold colloids likely occurred and promoted the formation of visible gold.

Keywords Visible gold deposition · Pyrite · Geochemistry · Jiaodong gold province · Microtextural analyses

Supplementary Information The online version contains supplementary material available at https://doi.org/10.1007/s11631-025-00833-3.

✉ Ting-Guang Lan
lantingguang@mail.gyig.ac.cn

[1] State Key Laboratory of Critical Mineral Research and Exploration, Institute of Geochemistry, Chinese Academy of Sciences, No.99 West Lincheng Road, Guiyang 550081, Guizhou Province, China

[2] School of Business Administration, Guizhou University of Commerce, Guiyang 550014, China

[3] Institute of Geology and Geophysics, Chinese Academy of Sciences, Beijing 100029, China

[4] Analysis Center, Tsinghua University, Beijing 100084, China

[5] MNR Key Laboratory of Gold Mineralization Processes and Resources Utilization, Shandong Institute of Geological Sciences, Jinan 250013, Shandong, China

1 Introduction

Gold in hydrothermal deposits can be recognized as "visible gold" and "invisible gold" (Saunders and Schoenly 1995; Groves et al. 1998; Reich et al. 2005; Sung et al. 2009; Saunders and Burke 2017). The former is prevalent in numerous hydrothermal gold deposits, such as orogenic and epithermal types, while the latter is commonly found in the Carlin type (White and Hedenquist 1995; Groves et al. 1998; Saunders and Burke 2017). The world-class Jiaodong gold province in China, hosting over 5000 t of

gold resources within an area of < 20,000 km^2, is characterized by visible gold mineralization (Qiu et al. 2002; Goldfarb and Santosh 2014; Groves and Santosh 2016; Peng et al. 2021). Visible gold in this province is commonly associated with pyrite, occurring as free grains, inclusions, or along pyrite grain boundaries (Yang et al. 2016; Li et al. 2018; Deng et al. 2020). Although previous studies have linked the gold mineralization to fluid boiling or fluid-rock interaction (Fan et al. 2007; Wen et al. 2015; Guo et al. 2017; Deng et al. 2020), the specific mechanisms governing visible gold formation remain poorly understood. The presence of high-grade visible gold means highly efficient precipitation of Au, which is difficult to explain using conventional theories that Au is precipitated directly from a solution (Petrella et al. 2020; Hastie et al. 2021; McLeish et al. 2021), due to the low solubility of Au (less than 100 ppb) in the fluids responsible for gold mineralization (Simmons and Brown 2006; Williams-Jones et al. 2009; Rauchenstein-Martinek et al. 2014; Wagner et al. 2016; Hastie et al. 2020; Wang et al. 2022). Therefore, there may be some disequilibrium processes leading to the highly efficient deposition of Au in the Jiaodong gold province.

Gold deposits in the Jiaodong gold province are primarily classified into two mineralization styles: the quartz-vein type (also known as Linglong type) and the altered-rock type (Jiaojia type) (Qiu et al. 2002). Both share similarities in mineralogy, lithology, geochronology, alteration assemblages, ore-forming fluids, and ore genesis, despite their differences in mineralization style (Qiu et al. 2002; Fan et al. 2007; Wen et al. 2015; Guo et al. 2017; Deng et al. 2020). The quartz-vein type is characterized by high-grade auriferous quartz-sulfide veins, while the altered-rock type is characterized by disseminated and stockwork mineralization with low grade and large scale. Different hydrothermal stages of the quartz-vein type are easy to recognize, making them ideal for studying the fluid evolution and detailed processes controlling the formation of visible gold. The world-class Linglong gold deposit is a typical quartz vein-type mineralization and one of the largest (over 150 t Au resource) and highest-grade (up to hundreds of grams per ton, g/t) gold deposits in the Jiaodong gold province (Wen et al. 2015; Guo et al. 2017; Wang et al. 2022; Xue et al. 2025). The hand samples collected from this deposit in the past exhibit a significant presence of visible gold to the naked eye (Fig. 1). Hence, this deposit provides a well site to investigate the highly efficient deposition of Au.

Pyrite is the most abundant sulfide mineral in the Jiaodong gold province, serving as a host for the visible gold

Fig. 1 Photograph of high-grade ores from the Linglong gold deposit showing that gold is heterogeneously distributed in quartz-pyrite veins. The yellow arrows mark the gold grains. The photo was taken with the permission of the Gold Mining Museum in Zhaoyuan City, Shandong Province

(Deng et al. 2020; Li et al. 2021; Yuan et al. 2021). It plays a crucial role in Au mineralization and can provide valuable insights, via its microtextural characteristics and trace elemental and sulfur isotopic geochemistry, into the evolution of ore-forming fluids and Au precipitation mechanisms (Deditius et al. 2014; Peterson and Mavrogenes 2014; Syverson et al. 2015; Fougerouse et al. 2016a, b; Tardani et al. 2017; Li et al. 2018; McLeish et al. 2024). In this study, we conducted detailed microtextural analyses using polarizing microscope and scanning electron microscopy (SEM), trace elemental analyses using laser ablation-inductively coupled plasma-mass spectrometry (LA-ICP-MS) and time-of-flight secondary ion mass spectrometry (TOF–SIMS), and sulfur isotopic analyses using laser ablation-multiple collector-inductively coupled plasma-mass spectrometry (LA-MC-ICP-MS) on auriferous pyrite from the Linglong gold deposit, to decipher the microtextural and geochemical evolution of pyrite and ultimately unravel the key processes governing visible gold formation in the Jiaodong gold province.

2 Geological setting

2.1 Regional geology

The Jiaodong Peninsula is located in Eastern China. It is bordered to the west by the Tan-Lu fault belt, to the north by the Bohai Sea, and to the east and south by the Yellow Sea (Fig. 2). It tectonically consists of the Jiaobei and Sulu Terranes in the west and east, respectively. The Jiaobei Terrane belongs to the southeastern region of the North China Craton. It can be further subdivided into the Jiaobei uplift and Jiaolai basin in the north and south, respectively. The Sulu Terrane belongs to the eastern part of the Dabie-Sulu

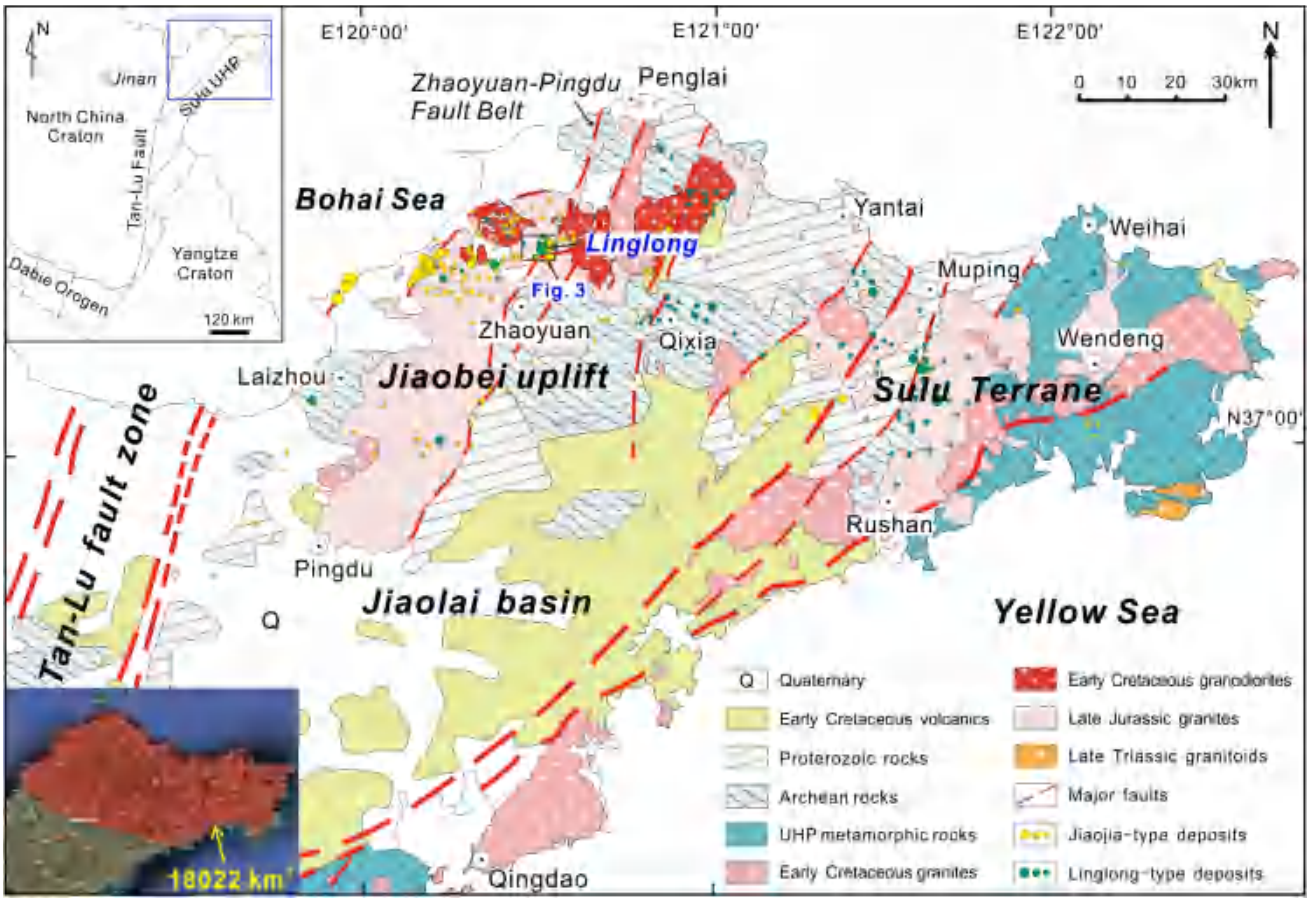

Fig. 2 Simplified geological map of the Jiaodong gold province and the distribution of main gold deposits (after Wen et al. 2016)

Orogen, which is widely considered to be the Triassic suture zone between the North China and Yangtze cratons (Li et al. 2012; Zheng et al. 2019). The Precambrian basement of the Jiaodong Peninsula is mainly composed of trondhjemite–tonalite–granodiorite gneisses and regional metamorphic rocks (Wan et al. 2006; Jahn et al. 2008; Deng et al. 2020). Mesozoic granites, primarily formed during the Late Jurassic (160–150 Ma) and Early Cretaceous (120–100 Ma), are the most widespread intrusions in the Jiaodong Peninsula (Hou et al. 2007; Goss et al. 2010; Yang et al. 2012). Early Cretaceous granodiorites (130–126 Ma) are considered to have a close temporal relationship with gold mineralization and mainly developed in the Jiaobei uplift (Jiang et al. 2016; Zhang et al. 2020). Basaltic to rhyolitic volcanics, which erupted during 118–93 Ma, are mainly distributed in the Jiaolai basin (Ling et al. 2007). Cretaceous intermediate-mafic rocks (mainly lamprophyre and diabase) are widespread as dikes in the Jiaodong Peninsula (Cai et al. 2013, 2015; Deng et al. 2017; Liang et al. 2017). Ultrahigh- to high-pressure metamorphic rocks, which formed during the Late Triassic (240–225 Ma), occur in the Sulu Terrane (Wu and Zheng 2013; Deng et al. 2020).

2.2 Deposit geology

Gold deposits in the Jiaodong gold province occur mainly within the Jiaobei uplift (Fig. 2) and were predominantly formed at 120 ± 2 Ma (Zhang et al. 2020, and references therein). The orebodies are mainly hosted in the Mesozoic granitoids and controlled by NE- to NNE-trending faults. The mineralization occurs predominately as Au-bearing quartz-sulfide lodes filled in the open fractures (quartz-vein type) and disseminations and stockworks in the altered rocks (altered-rock type) (Qiu et al. 2002; Wen et al. 2015; Guo et al. 2017). The quartz vein-type mineralization is smaller in scale, higher in grade, and steep-dipping in orebodies (> 60°). By the contrast, the altered rock-type orebodies are less steep (< 45°) with larger scale and lower grade (Qiu et al. 2002; Song et al. 2015).

The Linglong gold deposit is located at the north of the Jiaobei uplift (Fig. 2). It is of typical quartz vein-type mineralization and one of the most famous deposits in the Jiaodong Peninsula. It was formed at 120 ± 2 Ma (Yang and Zhou 2001; Zhang et al. 2020). There are over 200 auriferous quartz-sulfide veins (Fig. 3), which are dominantly hosted in the Late Jurassic Linglong granite (166–149 Ma;

Zhang et al. 2020, and references therein). The ore veins are controlled by the secondary NE-trending faults of the Zhaoyuan-Pingdu fault. It is clearly identified that four hydrothermal stages are developed in the Linglong gold deposit based on mineral paragenesis and crosscutting relationships (Wen et al. 2015; Guo et al. 2017; Wang et al. 2022). Stage I is characterized by massive gold-barren quartz that is commonly milky white (Figs. 1 and 4a) and homogeneous in texture (Wang et al. 2022). Stage II is characterized by the assemblage of gold + quartz + pyrite (Py1). This stage commonly shows smoky gray quartz and abundant pyrite aggregates (Fig. 4b). Quartz is anhedral or fine-grained, within which abundant fine pyrite grains are scattered (Fig. 4b–d). Gold generally occurs in pyrite aggregates in stage II (Fig. 4b, f). Stage III is characterized by the assemblage of quartz + polymetallic sulfides (chalcopyrite, sphalerite, and galena) + pyrite (Py2). Pyrite and quartz of this stage are generally euhedral grained, with their interstices being occupied by massive chalcopyrite, sphalerite, and galena (Fig. 4e). Stage IV is characterized by gold-barren quartz-calcite veinlets and marks the end of hydrothermal mineralization.

3 Sampling and analytical methods

3.1 Sampling strategy

Twenty-five samples were collected from the Xishan mining area. Representative samples containing abundant visible gold and sulfides collected from the underground tunnel (–50 m depth; Fig. 4a) were selected for analysis in this study. The samples were prepared into polished thin sections for SEM, LA-ICP-MS, TOF–SIMS, and LA-MC-ICP-MS analyses.

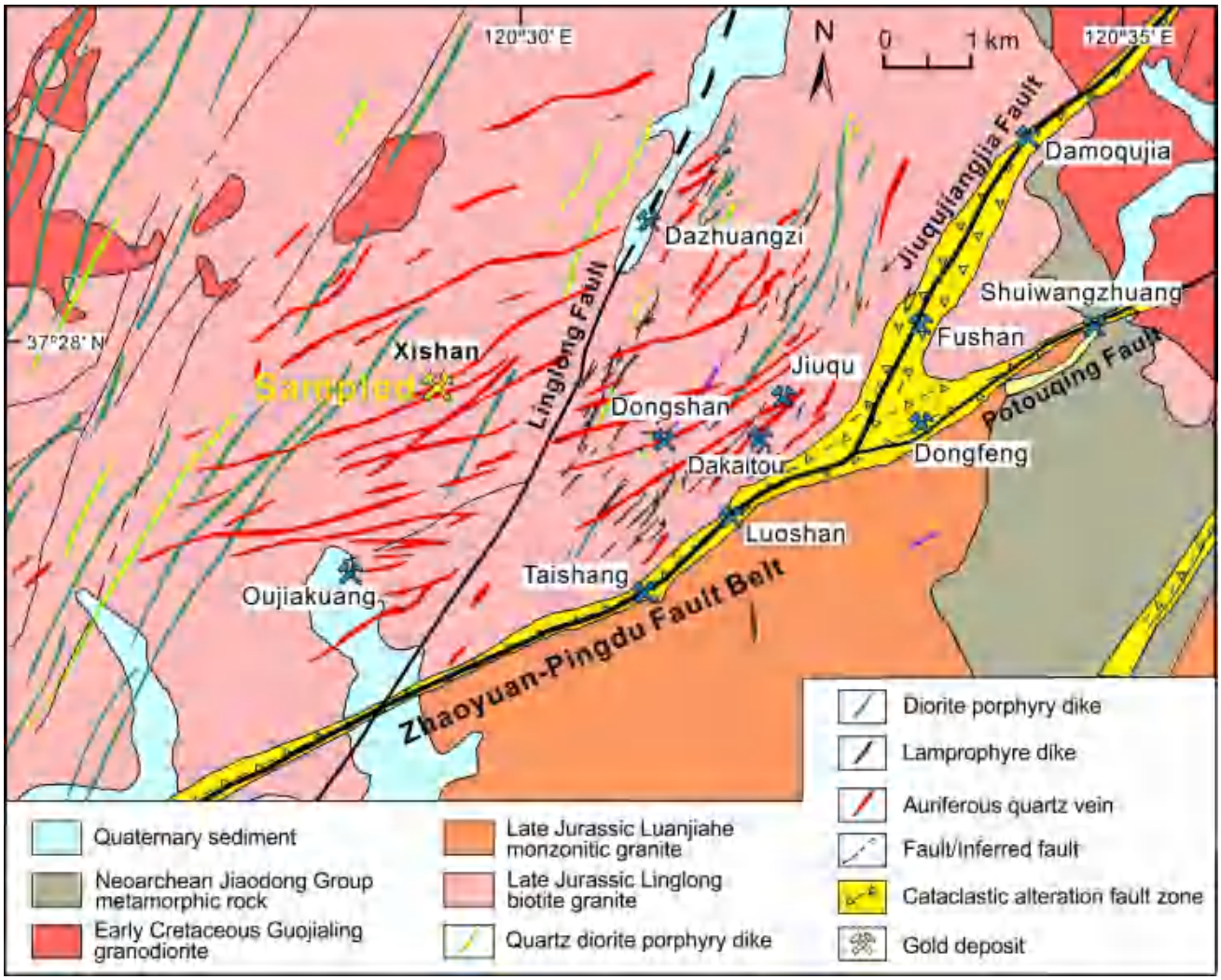

Fig. 3 Simplified geological map of the Linglong gold deposit (after Guo et al. 2017)

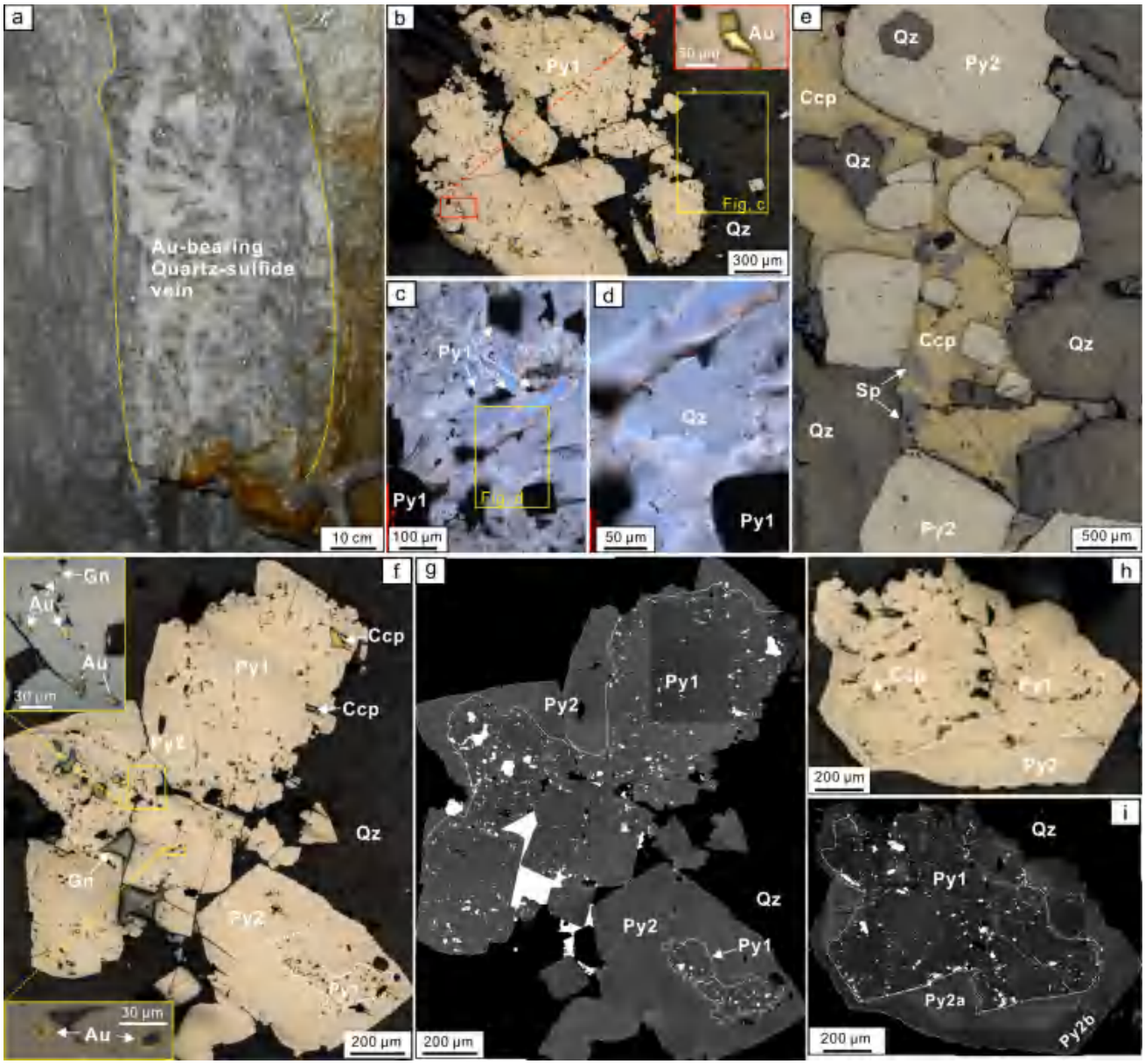

Fig. 4 Photographs of the ore vein and mineral assemblages. **a** Gold-bearing quartz-sulfide veins. **b** Py1 aggregates (hydrothermal stage II) containing visible gold and abundant sulfide inclusions. **c** and **d** Quartz near Py1 aggregates containing abundant Py1 inclusions. **e** Py2 (hydrothermal stage III) occurring as euhedral crystals and coexisting with euhedral quartz. **f** and **h** Py2 overprinting Py1. **g** and **i** Backscattered electron (BSE) images of (**f**) and (**h**). Au. visible gold, Ccp. chalcopyrite, Gn. galena, Py. pyrite, Qz. quartz, Sp. sphalerite

3.2 SEM analysis

SEM analyses were conducted at the State Key Laboratory of Critical Mineral Research and Exploration (SKLCMRE), Institute of Geochemistry, Chinese Academy of Sciences (IGCAS). The analyses were carried out with a working distance of 10 mm, an incident current of 10 nA, and an accelerating voltage of 10–20 kV.

3.3 LA-ICP-MS elemental analysis

Trace element concentrations of pyrite were obtained by LA-ICP-MS at the SKLCMRE, IGCAS. Laser sampling and mass spectrometry analyses were accomplished with a RESOlution S-155 ArF193-nm laser ablation system and an Agilent 7700x quadrupole ICP-MS, respectively. The carrier gas was helium (370 ml/min) and the transport gas was argon (900 ml/min). Each spot analysis comprised 20 s, 60 s,

and 40 s for background acquisition, data acquisition from samples, and elimination of memory effects, respectively. Analyses were conducted with the following parameters: laser fluence of 3.5 J/cm^2, beam size of 26 μm, and laser beam repetition rate of 6 Hz. For calibration of elemental concentrations, standards GSE-1G, GSD-1G, and STDGL3 were analyzed (Belousov et al. 2023). To check the analytical accuracy, MASS-1 (sulfide reference material) was analyzed as an unknown sample (Wilson et al. 2002). Iolite software was used to process the data (Paton et al. 2011). It should be noted that the concentrations of trace elements in pyrite were calculated from the LA-ICP-MS data showing smooth time-resolved spectra. The data exhibiting obvious spikes, particularly those for Au–Ag or Cu–Zn–Pb–Bi–Ag, were calculated as the elemental concentrations of mineral inclusion-bearing pyrite for reference only.

LA-ICP-MS elemental mapping of pyrite was performed through ablation of parallel lines in a grid pattern with the following parameters: laser fluence of 3.5 J/cm^2, beam size of 15 μm, laser beam repetition rate of 15 Hz, line spacing of 15 μm, and scanning speed of 15 μm/s. The standards STDGL3 and GSE-1G were analyzed once before and after each sample to correct for instrument mass bias. Iolite software was used to process the data.

3.4 TOF–SIMS analysis

High-resolution element-distribution mapping of pyrite was performed with an IONTOF TOF–SIMS 5 spectrometer at the Analysis Center, Tsinghua University. A 30 keV bismuth liquid metal ion gun was used as the primary ion source. Bi_1^+ was selected as primary ion by appropriate mass filter settings. The Bi_1^+ current was about 10 pA (1 ns pulse width, bunched beam). Images were acquired over a 500 μm × 500 μm area and a 300 μm × 300 μm area at 256 × 256 pixels in random raster mode. Both positive and negative ion modes were employed to examine ions or ion clusters within a mass range of approximately 0–1000 amu. Prior to the measurement, a 2 keV Cs^+ beam was used as a sputter gun to clean the surface of the samples.

3.5 LA-MC-ICP-MS sulfur isotope analysis

In situ sulfur isotopic analyses of pyrite were conducted with LA-MC-ICP-MS at the SKLCMRE, IGCAS. The analyses were conducted near the spots which had been conducted for elemental analyses with LA-ICP-MS to determine the coupled elemental and isotopic compositions. Laser sampling and mass spectrometry analyses were accomplished with the RESOlution S-155 ArF 193-nm laser ablation system and a Nu Plasma III MC-ICP-MS, respectively. Each spot analysis comprised 20 s, 40 s, and 40 s for background acquisition, data acquisition from samples, and elimination of memory effects, respectively. Analyses were conducted with the following parameters: laser fluence of 3 J/cm^2, beam size of 40 μm, and repetition rate of 5 Hz. For mass bias correction, an external standard (pressed pyrite powder tablet, PSPT-2) was repeatedly measured every five unknown samples (Bao et al. 2017; Chen et al. 2019). For quality control, two in-house pyrite standards (natural crystals, SB-1 and HYC-1) were analyzed as unknown samples (Wang et al. 2024). The measured $\delta^{34}S_{V\text{-}CDT}$ values were 16.67‰ ± 0.48‰ (2SD, $n = 16$) for SB-1 and −5.58‰ ± 0.31‰ (2SD, $n = 16$) for HYC-1, which are agreement with the recommended values (SB-1: 16.57‰ ± 0.20‰; HYC-1: −5.76‰ ± 0.20‰) within error ranges.

4 Results

4.1 Types and microtextures of pyrite

According to mineral assemblage, crosscutting relationship, and pyrite microtexture and morphology, two main types of pyrite have been identified in this study. Pyrite grains of type I (Py1) occur as aggregates distributed in the quartz-pyrite veins (hydrothermal stage II; Fig. 4b). They are composed of multiple euhedral to subhedral, medium- to fine-grained crystals (Figs. 4 and 5). The reflected-light microphotographs and SEM backscattered electron (BSE) images show that Py1 is "unclean" and contains abundant pores and microfracture-fillings or inclusions of galena, sphalerite, and chalcopyrite tens of microns in size (Figs. 4b, f–i, and 5). The SEM secondary electron (SE) images show that the pores are gaps in the junctions among multiple fine grains of pyrite that retain primary euhedral shapes (Fig. 5k, l).

Type-II pyrite (Py2) is commonly coarse- to medium-grained and euhedral to subhedral. They occur in isolation within the pyrite-chalcopyrite-sphalerite-galena veins (hydrothermal stage III) (Fig. 4e), or overprint Py1 in the quartz-pyrite veins (Fig. 4f–i). Py2 is homogeneous in texture, within which mineral inclusions and Au grains are rarely found. In BSE images, the backscattered brightness of Py2 is stronger than that of Py1, but decreases sharply in the rims of some grains (Fig. 4i). Consequently, Py2 can be further divided into two subtypes: the BSE-bright Py2a and BSE-gray Py2b.

4.2 Occurrence of visible gold

The gold grains are commonly ellipsoidal with sizes of tens of microns (Figs. 4f and 5). They are generally distributed in isolation within Py1 aggregates. In a few cases, gold grains coexist with galena or chalcopyrite (Figs. 4b and 5n). The reflected-light microphotographs show that some gold

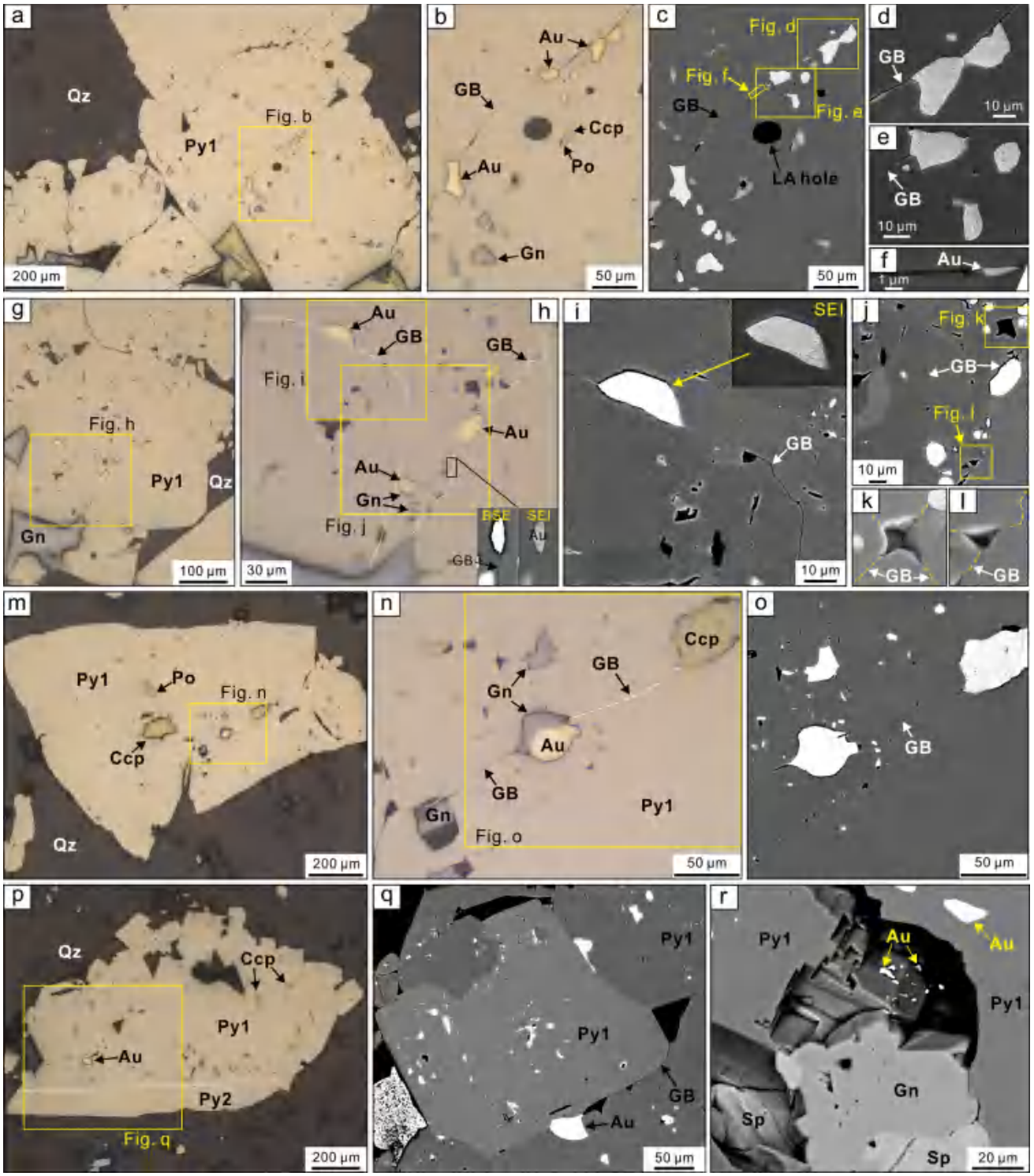

Fig. 5 Optical and electron microscope photos showing occurrence of visible gold. **a** and **b** Reflected-light photos showing gold grains distributed along Py1 grain boundaries. **c** Backscattered electron (BSE) image of (**b**). **d** and **e** Secondary electron (SE) images showing coarse-grained gold along Py1 grain boundaries. **f** SE image showing a submicron particle of gold in the gap between two Py1 grains. **g–j** Py1 grain boundaries disappear in the reflected-light photomicrographs, but appear in the BSE images (**i** and **j**). **k** and **l** SE images showing gaps at the junctions among multiple primary grains of Py1. **m–o** Coexisting gold and galena distributed along Py1 grain boundaries. **p** Py1 grain boundaries disappear in the reflected-light photomicrographs. **q** BSE image shows clearly euhedral pyrite crystals within Py1 aggregates, and gold is distributed along the Py1 grain boundaries. **r** Fine-grained gold deposited on the surface of euhedral pyrite within Py1 aggregate. Au. visible gold, Ccp. chalcopyrite, GB. grain boundary, Gn. galena, Po. Pyrrhotite, Py. pyrite, Qz. quartz, Sp. sphalerite

grains are distributed along boundaries between crystals of Py1 (Fig. 5a, b, n). These Py1 crystals are euhedral cubic and undeformed with straight boundaries. In some cases, although the boundaries of pyrite crystals disappear and gold grains seem to occur as inclusions within pyrite under reflected-light microscopy (Fig. 5g, p), SEM-BSE images distinctly reveal that the pyrites maintain regular boundaries within aggregates, and gold grains are distributed along these boundaries (Fig. 5i, j, q). Some submicron-scale gold grains are found in the nanoscale gaps between two pyrite grains (Fig. 5f) or on the surface of euhedral fine-grained pyrite within Py1 aggregates (Fig. 5r).

4.3 Trace element content of pyrite

The LA-ICP-MS time-resolved depth profiles of Py1 are either smooth or spiked (Fig. 6a–c). The domains of Py1 without mineral inclusions show smooth profiles with low counts of most elements (Fig. 6a). By contrast, the domains with mineral inclusions show spiked profiles, in which the spectra are rarely flat and are parallelly spiked for some metals, such as Cu–Zn–Pb–Bi–Ag (Fig. 6b), and Au–Ag (Fig. 6c). The profiles of Py2 are consistently flat, in which the spectra of As are significantly strong and are parallel to the stable spectra of Au (Fig. 6d), suggesting the higher and relatively stable concentrations of As and Au.

The quantitative calculation results of trace elements in different pyrites are listed in Supplementary Table S1. Cobalt, Ni, Cu, Zn, As, Pb, Bi, Ag and Au are commonly detectable, but vary widely in concentration in the two types of pyrite. Copper, Zn, Ag, Pb, and Bi are relatively enriched in Py1, while As, Au, and Co are higher in Py2 (Fig. 7a). The median concentration of Au in Py2 is 0.304 ppm, which is an order of magnitude higher than that in Py1 (0.032 ppm). Significantly, the median concentration of As in Py2 (2620 ppm) is three orders of magnitude higher than that in Py1 (8.77 ppm). The concentrations of Au and As are positively correlated with each other in Py2 ($r = 0.7042$), but show a weak correlation in Py1 (Fig. 7b). Gold shows better positive correlations with Ag, Cu, Zn, Pb, and Bi in Py1 relatively to Py2 (Fig. 7c–g). The two types of pyrite do not show a clear correlation between the concentrations of Co and Ni, but display similar Co/Ni ratios (Fig. 7h).

LA-ICP-MS element mapping offers a more intuitive representation of the distributions and spatial correlations of various elements within different pyrites (Fig. 8). The results show that As and Au are significantly concentrated in Py2, especially in the BSE-bright Py2a. In contrast to Au, Ag is depleted in Py2 but more concentrated in Py1 and distributed similarly to the Cu-, Pb-, and Zn-bearing inclusions. Cobalt is concentrated in or near the boundaries between Py2a and Py2b, or in the healed microcracks of Py1. Nickel is uniformly depleted in Py1 but relatively enriched in Py2.

High-resolution elemental mapping with TOF–SIMS was conducted to further identify the relationships between visible gold and pyrite. Both positive and negative ion

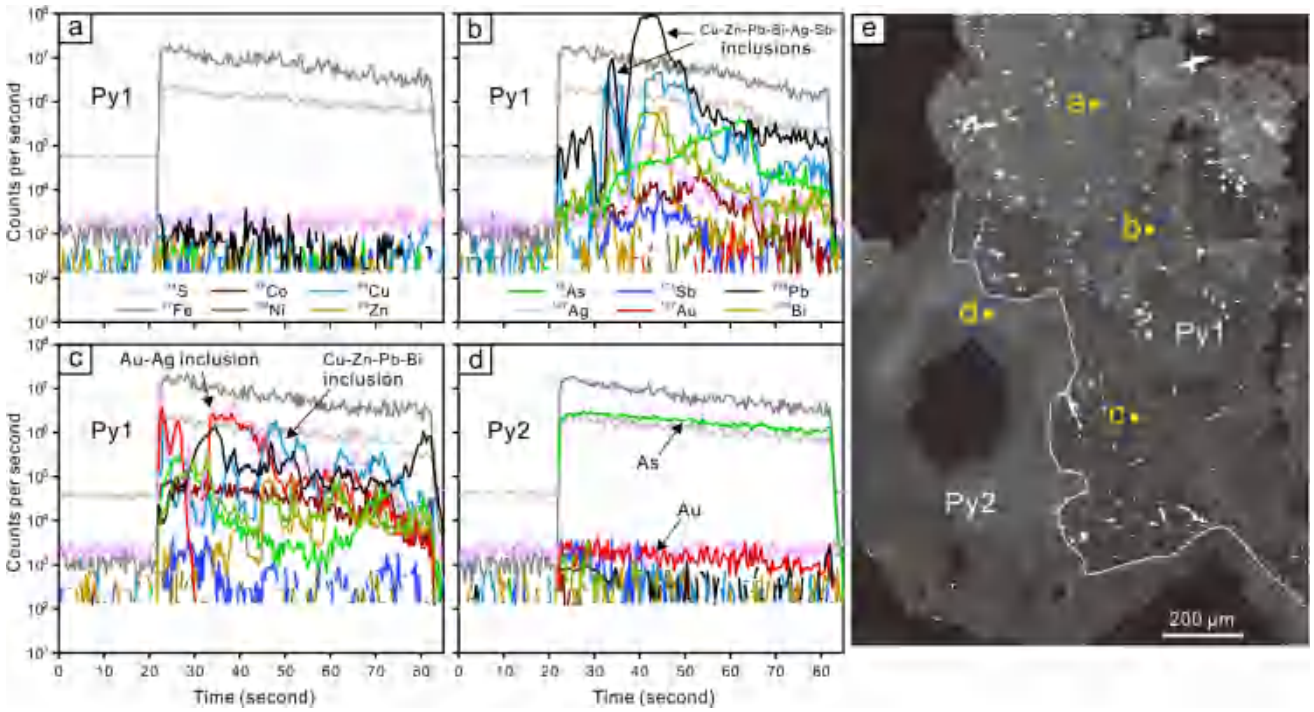

Fig. 6 Representative LA-ICP-MS time-resolved depth profiles for different types of pyrite (**a**–**d**) and their laser ablation locations (**e**)

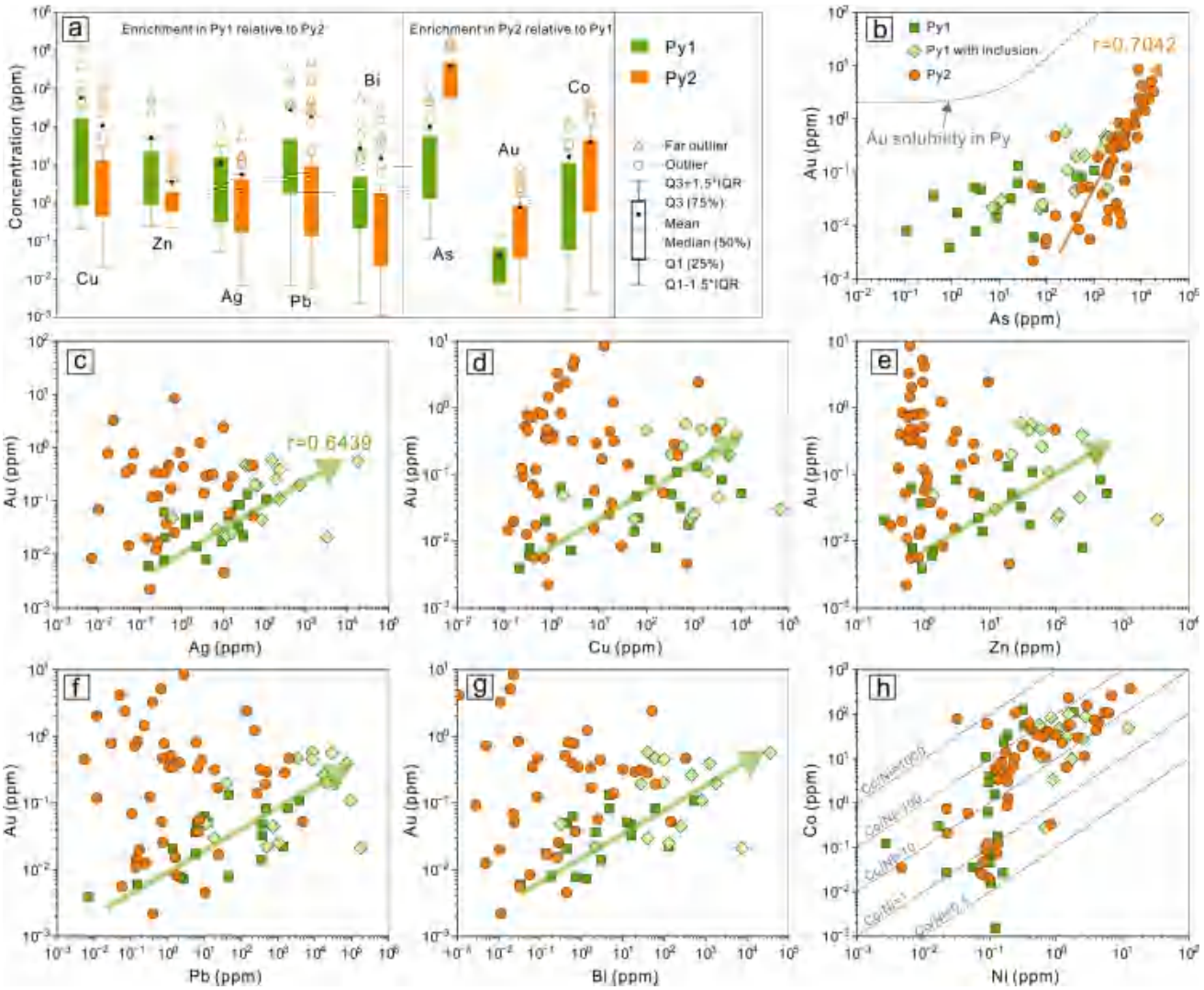

Fig. 7 Comparative box (**a**) and binary (**b**–**h**) plots showing the concentrations of selected trace elements in different types of pyrite. The concentrations shown in the box plot were calculated based on LA-ICP-MS data with flat time-resolved spectra, excluding the data of Py1 containing obvious electrum or Cu–Zn-Pb-Bi-Ag-bearing inclusions. The concentrations shown in the binary plots include the data of mineral inclusion-bearing Py1

modes were attempted to test multiple elements and/or ion clusters. However, only the distribution of As^- and AsS^- in pyrite obtained in the negative ion mode are available, which comprehensively show that As is relatively enriched in the BSE-bright Py2a (Fig. 9), consistent with the above LA-ICP-MS analyses. The signal of Au is absent within pyrite in both positive and negative ion modes, probably owing to its low concentrations. The distribution of Au^- obtained in the negative ion mode just displays the distribution of visible Au (Fig. 9g, j). The high-resolution AsS^- and Au^- maps, combined with BSE images, comprehensively confirm that the visible gold is distributed along the boundaries between As-depleted Py1 grains (Fig. 9d–k).

4.4 Sulfur isotopic compositions of pyrite

The in situ $\delta^{34}S$ values of Py1 are within a narrow range of 4.86‰–6.75‰. For Py2, the $\delta^{34}S$ values are more varied and are commonly higher than those of Py1 (Fig. 10a, b), showing the results of 5.25‰–10.14‰. Within Py2 grains, the $\delta^{34}S$ values show a progressive increase outward from Py2a to Py2b (Fig. 10c, d). There is no significant correlation between the sulfur isotopic and trace elemental compositions of the two types of pyrite. The detailed data are listed in Supplementary Table S1.

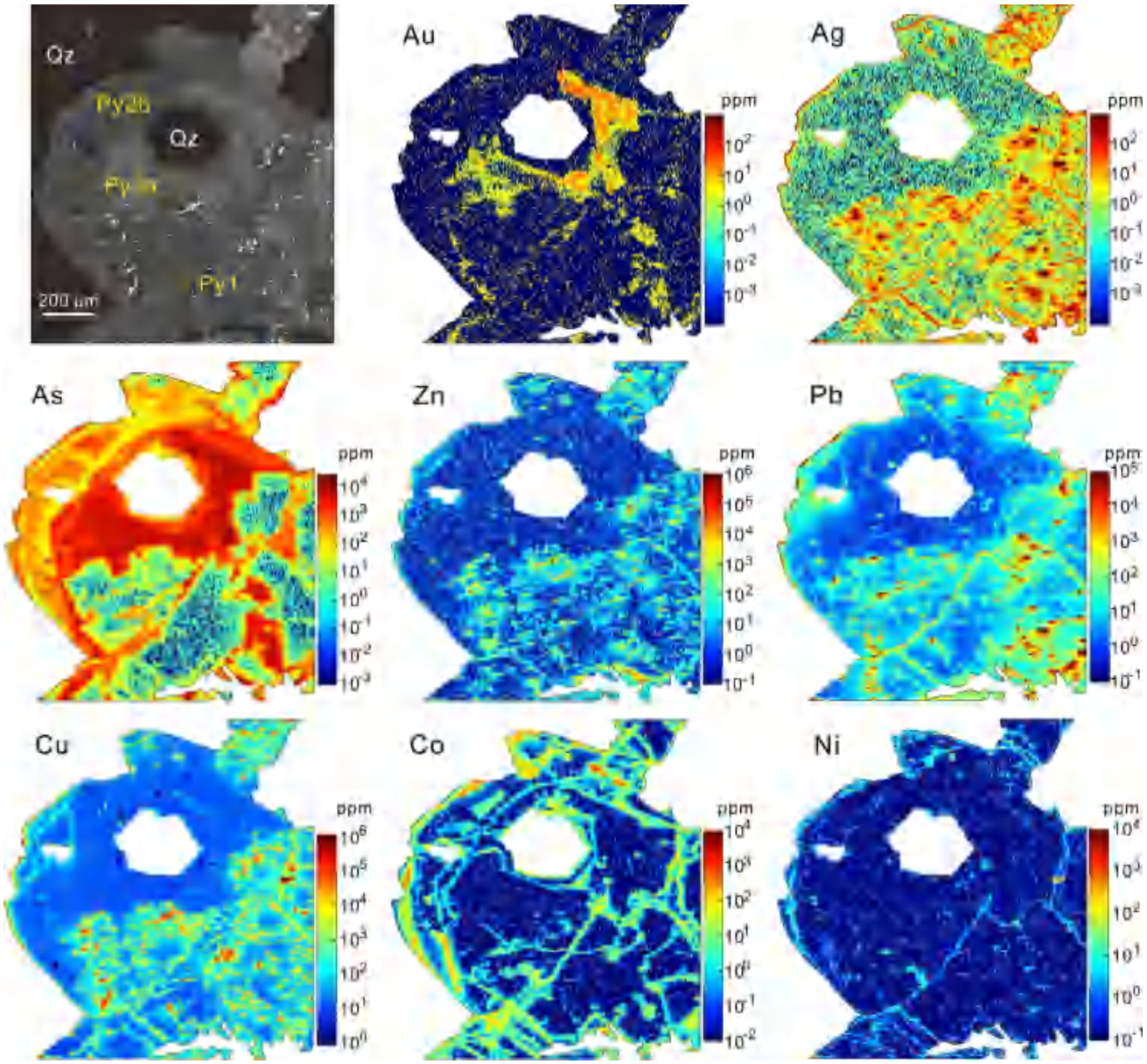

Fig. 8 Backscattered electron (BSE) image and LA-ICP-MS elemental mapping of pyrite showing the distribution of Au, Ag, As, Zn, Pb, Cu, Co, and Ni

5 Discussion

5.1 Relationship between pyrite and visible gold

The occurrence of gold within pyrite can be either "visible" or "invisible" under optical microscopes (Reich et al. 2005; Sung et al. 2009; Deditius et al. 2014). In the former case, gold occurs as free gold-bearing minerals such as native gold, electrum, or Au-(Ag) tellurides (Cook et al. 2009; Ciobanu et al. 2012; Jian et al. 2021). "Invisible gold" can occur either as free gold-bearing nano- to submicron-scale particles (Au^0) within pyrite or as a solid solution (Au^+) in the pyrite lattice (Reich et al. 2005; Tauson et al. 2014; Hastie et al. 2020; Liang et al. 2021; Pokrovski et al. 2021). In the Linglong and other gold deposits of the Jiaodong gold province, the visible gold mainly occurs as native gold or electrum spatially related to pyrite, and contributes over 99% of the gold reserves (Mills et al. 2015; Wen et al. 2015; Yang et al. 2016; Peng et al. 2021). Thus, it is crucial to clarify the relationship between the visible gold and gold-bearing pyrite to decipher the formation process of visible gold. Usually, visible gold occurs in three forms in pyrite: (1) inclusion gold, (2) fissure gold, and (3) intergranular gold. In this study, the coarse gold grains are typically distributed

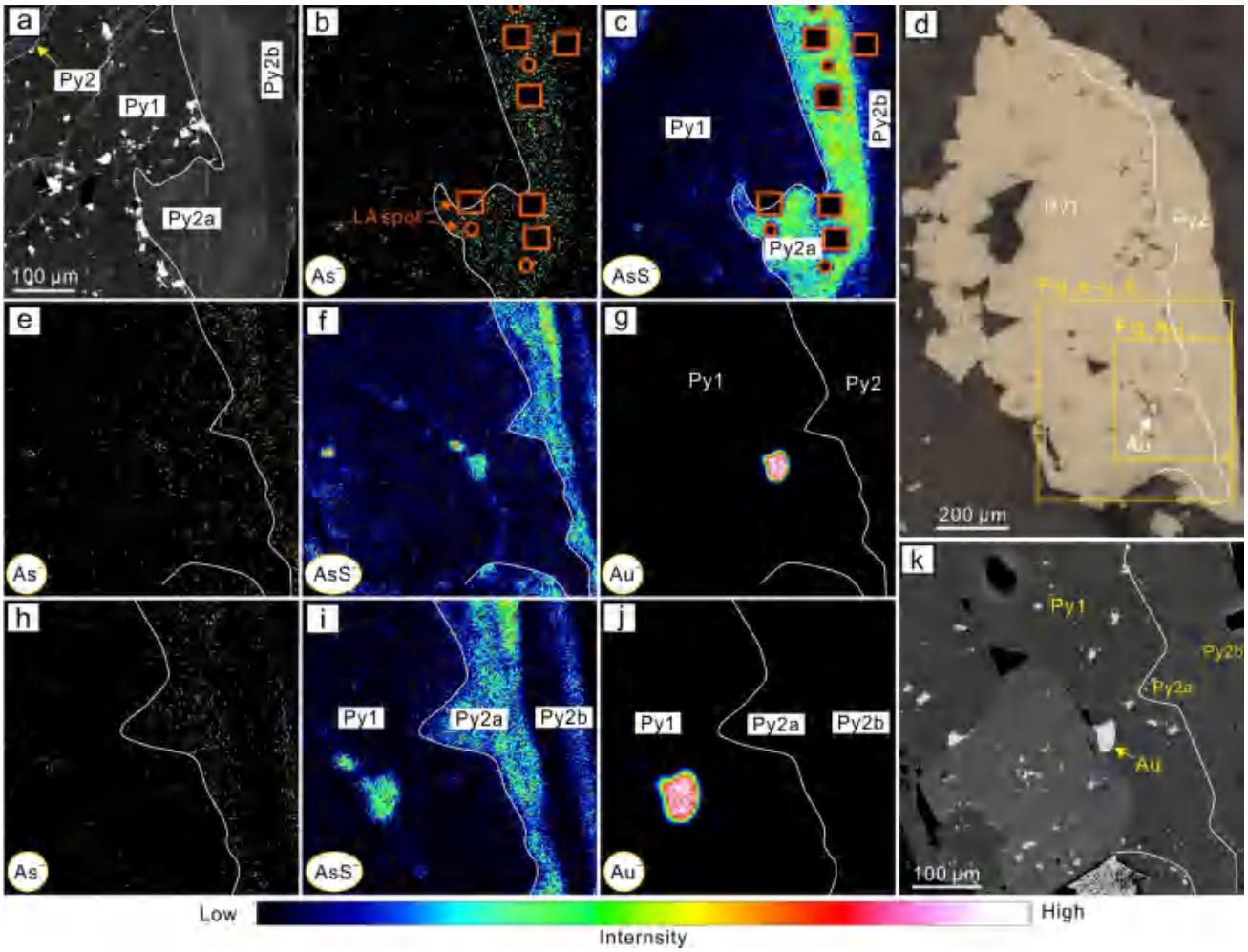

Fig. 9 Time-of-flight secondary ion mass spectrometry (TOF–SIMS) mapping of pyrite

along the boundaries of pyrite grains within Py1 aggregates in the reflected-light microphotographs (Fig. 5a, b, n). The Py1 crystals are euhedral cubic crystals and undeformed, showing straight boundaries near gold grains. Thus, the gold grains are intergranular gold rather than inclusion or fissure gold. Although some gold grains appear to be inclusion gold under reflected light (Fig. 5g, p), they are actually distributed along pyrite boundaries in the SEM images (Fig. 5i, j, q) and are in fact intergranular gold. The submicron-scale gold grains occurring in the nanoscale gaps between two pyrite grains (Fig. 5f) or on the surface of euhedral fine-grained pyrite (Fig. 5r) also indicate that the visible gold occurs as intergranular particles within Py1 aggregates.

Py2 crystals are generally larger (Fig. 4) and relatively enriched in invisible Au (Fig. 7a). However, there is no visible gold found within Py2 crystals under optical and electron microscopy (Fig. 4). The TOF–SIMS maps also provide robust evidence that visible gold is closely associated with Py1 rather than Py2 (Fig. 9). Some studies on other gold deposits in the Jiaodong gold province have also demonstrated that the most important host mineral of gold is the pyrite of the quartz-pyrite stage (stage II) rather than that of the quartz-polymetallic sulfide stage (stage III) (Li et al. 2021; Yuan et al. 2021). Thus, it can be inferred that the visible gold was predominately formed during hydrothermal stage II.

5.2 Occurrence of invisible gold

As discussed above, gold occurs predominantly as visible gold associated with pyrite of hydrothermal stage II. Nevertheless, determining whether the "invisible gold" in pyrite occurs as a solid solution or nanoparticles could provide insights into the formation process of visible gold. Although Au concentrations in this study are below the upper limit of Au solubility in pyrite (Fig. 7b) (Reich et al. 2005), the occurrence of invisible (nano- to submicron-scale) particles of gold or electrum (Au^0) within pyrite

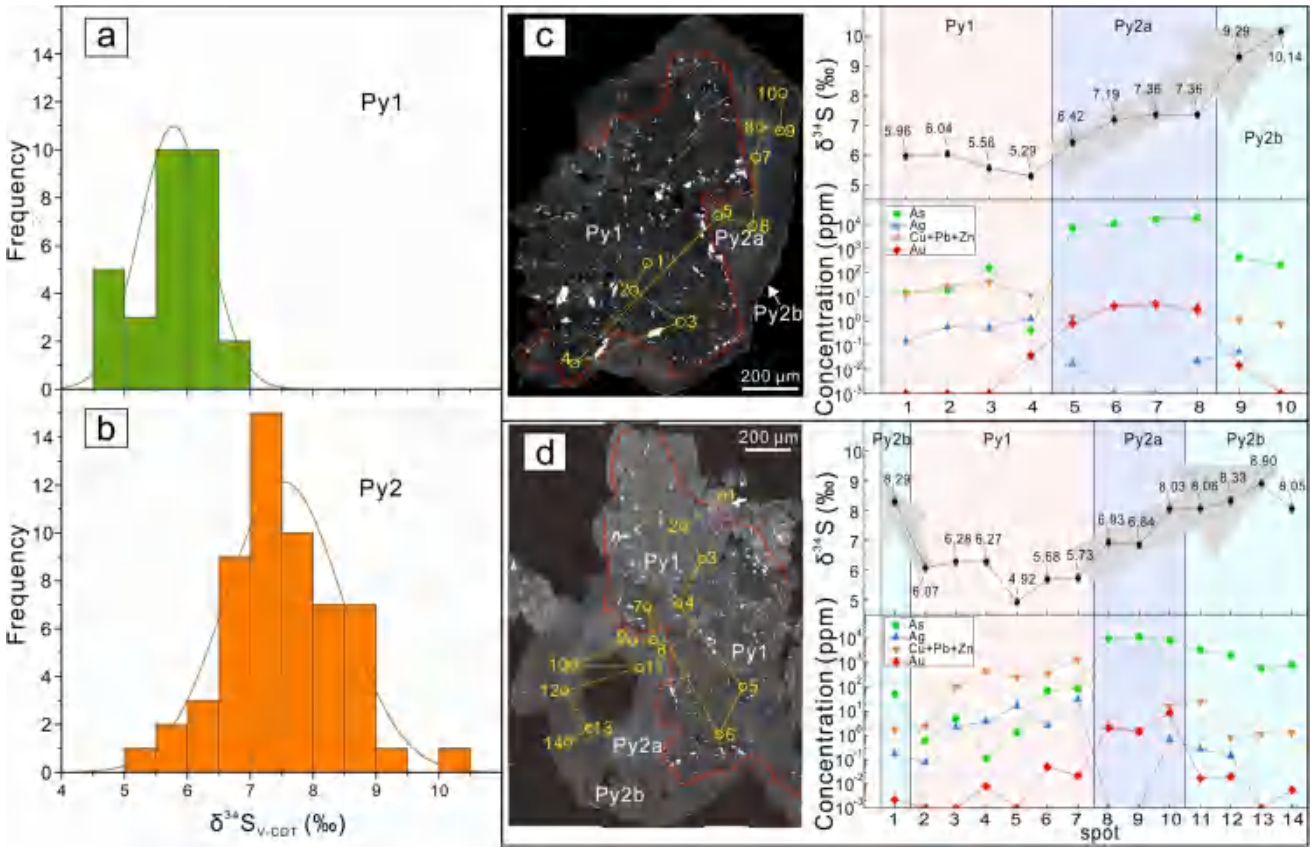

Fig. 10 Sulfur isotopic compositions of pyrite in this study. **a** and **b** Histograms of $\delta^{34}S_{V\text{-}CDT}$ values of Py1 and Py2. **c** and **d** Backscattered electron (BSE) images of pyrite and the corresponding $\delta^{34}S_{V\text{-}CDT}$ values and selected trace element concentrations

cannot be ruled out. The parallel spikes of Au and Ag signals in LA-ICP-MS time-resolved depth profiles of Py1 indicate the presence of invisible particles of electrum (Fig. 6c), which is also supported by the positive correlation ($r = 0.6439$) between Au and Ag concentrations in Py1 (Fig. 7c). Moreover, the relatively positive correlations between Au and elements such as Cu, Zn, Pb, and Bi in Py1 (Fig. 7d–g) imply that certain nano- to submicron-scale particles of gold and electrum coexist with Cu-, Pb-, and Zn-bearing minerals (chalcopyrite, galena, and sphalerite) of comparable size. This is consistent with the optical microscopic observations that some larger gold grains are coexistent with galena and chalcopyrite grains along the grain boundaries of Py1 (Figs. 4b and 5n). The distribution and content of the invisible gold particles are heterogeneous and limited, as evidenced by the absence of Au–Ag signals in the clean domains (Fig. 6a) and the low concentrations of Au and Ag (Fig. 7a), as well as the decoupling of Au–Ag distribution within Py1 aggregates (Fig. 8).

In Py2, the absence of clear correlations between Au and elements such as Ag, Cu, Zn, Pb, and Bi (Figs. 7 and 8) suggests that Au does not exist in the form of free gold-bearing nano- to submicron-scale minerals. It has been widely recognized that the degree of Au incorporation into pyrite lattice depends positively on As concentrations (Reich et al. 2005; Deditius et al. 2014; Kusebauch et al. 2019; Pokrovski et al. 2021). The higher As concentrations (Fig. 7a) and the positive correlation ($r = 0.7042$) between Au and As in Py2 (Figs. 7b and 8) suggest that Au mainly occurs as lattice-bound ionic Au^{+} in this pyrite, similar to that in the Carlin-type Au deposit (Reich et al. 2005; Pokrovski et al. 2021).

5.3 Processes controlling pyrite texture and geochemistry

The microtexture and geochemistry of pyrite record the evolutionary history of the fluids (Deditius et al. 2014; Peterson and Mavrogenes 2014; Fougerouse et al. 2016a, 2016b; Tardani et al. 2017; Li et al. 2018). The Py1 aggregates are anhedral to euhedral, porous, and rich in mineral inclusions such as chalcopyrite, sphalerite, and galena (Figs. 4 and 5). The quartz near Py1 is anhedral, fine-grained, and rich in inclusions of pyrite (Fig. 4b–d). Such

textures indicate the fast formation of pyrite and quartz under unstable conditions (Román et al. 2019; Falkenberg et al. 2021). This is also supported by the geochemistry of pyrite. The higher and positively correlated concentrations of Cu, Zn, and Pb in Py1 (Fig. 7) suggest that those metals predominantly occur as nano- to submicron-scale minerals such as chalcopyrite, galena, and sphalerite, which might be trapped into Py1 crystals or aggregates under a fast crystallization rate of pyrite and disequilibrium conditions (Román et al. 2019).

Py2 and the coexisting quartz are commonly euhedral, coarse-grained and clean in texture (Fig. 4e, f–i), and were likely formed under relatively steady conditions (Román et al. 2019; Falkenberg et al. 2021). The consistently flat LA-ICP-MS spectra (Fig. 6d) and high concentrations of As in Py2 (Fig. 7a) also indicate the slow growth rate of pyrite under steadier, near-equilibrium conditions. This is because a long duration of contact between pyrite and fluid can facilitate the incorporation of As into the pyrite lattice (Xing et al. 2019; Kutzschbach et al. 2024). Similar to As, the relatively higher concentrations of Co and Ni in Py2 (Fig. 8) also support the formation of this pyrite under near-equilibrium conditions, as the two elements are held strongly by the pyrite during fluid–pyrite interaction (Ulrich et al. 2011; Wang et al. 2024). The near-equilibrium conditions are also consistent with the $\delta^{34}S$ results. The experimental study conducted by Syverson et al. (2015) demonstrated that heavy sulfur isotopes are more likely to remain in H_2S (fluid) during the process of pyrite crystallization. This means that the pyrite precipitated under equilibrium or near-equilibrium conditions from a closed-solution system would exhibit an increase in $\delta^{34}S$ values over time (Syverson et al. 2015; Feng et al. 2020). Therefore, the gradually increasing trend from the core (Py2a) to the rim (Py2b) within a single Py2 grain (Fig. 10c, d) indicates the near-equilibrium crystallization of Py2 under steadier conditions. By contrast, the $\delta^{34}S$ values of Py1 are lower (4.86‰–6.75‰) and change little from the interior to the edge within a single pyrite crystal or aggregate (Fig. 10), which likely resulted from the smaller sulfur isotopic fractionation between pyrite and fluids within a short duration of time (Syverson et al. 2015). Thus, it is also suggested that the Py1 crystallized rapidly.

Previous studies have shown that the ore fluids of different hydrothermal stages at the Linglong Au deposit were the same type of fluids derived from the same source (Wen et al. 2015; Guo et al. 2017; Wang et al. 2022). This is consistent with the similar Co/Ni ratios (Fig. 7h) for the two generations of pyrite in this study (Tardani et al. 2017; Román et al. 2019). In addition, the $\delta^{34}S$ values of Py1 are similar to the lower limits of those of Py2 (Fig. 10), also indicating that the fluids depositing Py2 (hydrothermal stage III) continuously evolved from those depositing Py1 (stage I). Previous studies have illustrated that the gold-barren quartz of the early stage (I) is coarse-grained and homogeneous in CL texture, and the corresponding fluid inclusions have consistent gas/liquid ratios, indicative of stable physicochemical conditions (Wen et al. 2015; Wang et al. 2022). Therefore, the physicochemical conditions of the ore-forming fluids of the studied gold deposit were stable during the early stage (I), unstable and in disequilibrium during stage II, and more stable and near-equilibrium during stage III. The sharp changes in physicochemical conditions from hydrothermal stages I to III were likely triggered by boiling processes, which likely took place in hydrothermal stage II and led to loss of H_2S, H_2, CO_2 and other volatiles to the vapor phase (Román et al. 2019; Falkenberg et al. 2021). These processes controlled the rapid crystallization of Py1 with complex texture and trace elemental compositions (Figs. 5–6). On the other hand, the coarse, euhedral Py2 grains with homogeneous texture and near-equilibrium geochemistry were likely to crystallize under gentle boiling or non-boiling conditions (Román et al. 2019). As the visible gold is predominantly associated with Py1, it can be concluded that the fluid boiling processes resulted in the highly efficient deposition of gold as visible particles during hydrothermal stage II. The gentle boiling or non-boiling conditions during stage III controlled the invisible gold precipitation without economic value.

5.4 Deposition mechanism of visible gold during fluid boiling

Since Au is mainly transported as sulfur complexes in ore fluids (Pokrovski et al. 2009; Williams-Jones et al. 2009), gold is unlikely to precipitate earlier than the associated sulfides such as pyrite. In addition, if pyrite and gold were co-deposited, the pyrite should contain abundant invisible gold or fine-grained visible gold inclusions (Reich et al. 2005; Hochella et al. 2008; Zhou et al. 2021). However, our observations contradict this expectation. Therefore, there are two possible mechanisms for the formation of visible gold: (1) after the formation of Py1 aggregates, Au was remobilized from pyrite crystals to their edges or underwent rapid diffusion along the sub-grain boundaries of pyrite (Yuan et al. 2021; Xian et al. 2022); or (2) Au remained briefly in the fluids during the crystallization of Py1 and was subsequently deposited at the margins of Py1 grains prior to their aggregation. For the first possibility, Au was mobilized to the fracture or gap between two sub-grains of pyrite so that the visible gold occurred as veinlets along grain boundaries or fractures of pyrite (Xian et al. 2022), rather than as isolated ellipsoidal grains within pyrite aggregates (Fig. 5). Therefore, we favor the second mechanism. Although the first mechanism is not absolutely excluded (Xian et al. 2022), it does not appear to be the dominant mechanism for the formation of visible gold in the Linglong gold deposit, especially for the quartz vein-type ores.

Numerous studies on Jiaodong gold deposits have demonstrated that the quartz vein-type mineralization was controlled primarily by fluid boiling during hydrothermal stages II to III (Fan et al. 2007; Wen et al. 2015; Guo et al. 2017; Wang et al. 2022). However, this understanding is challenged by our new findings that the fluid boiling likely occurred and resulted in economic gold mineralization only during hydrothermal stage II. The gold grains found in quartz-polymetallic sulfide veins (hydrothermal stage III) in previous studies were likely inherited from stage II. The ore-forming fluids belong to the low-salinity, medium-temperature CO_2-rich H_2O-CO_2-NaCl-$H_2S \pm CH_4$ system (Wen et al. 2015; Guo et al. 2017; Deng et al. 2020; Wang et al. 2022), in which Au is transported as sulfur complexes, such as $Au(HS)_2^-$ or $Au(HS)^0$ (Pokrovski et al. 2009; Williams-Jones et al. 2009). The Au–S complexes would be destabilized by the loss of H_2S or S^{2-} induced by fluid boiling and the resultant fast crystallization of pyrite (Py1). There should be intermediary steps between the destabilization of the Au–S complexes and the formation of larger gold crystals. During these steps, Au remained briefly and was further enriched in the fluids near pyrite during pyrite crystallization. Based on the above findings, we propose an alternative mechanism for the formation of visible gold in the quartz vein-type Linglong gold deposit.

Gold colloidal particles (typically 1–1000 nm in diameter), which must be dispersed in a stable manner in the fluids, could be the intermediary steps in the formation of coarse gold grains (Saunders and Schoenly 1995; Shields et al. 2010; Saunders and Burke 2017; Saunders et al. 2020; McLeish et al. 2021). There are two possibilities for the formation of the gold colloids: (1) in situ formation triggered by fluid boiling, or (2) physical transport from a deep source (Hannington et al. 2016; Gartman et al. 2018; Saunders et al. 2020). The latter scenario is considered unlikely, as the ore-forming fluids were deeply derived from the lower crust (Deng et al. 2020; Lan et al. 2023) and would be unable to preserve the unstable colloids over the long-distance migration. Therefore, the gold colloids are more likely to form in situ. Many studies have demonstrated that fluid boiling can cause Au to drop out of solution and to become colloidal suspensions in the residual fluids (Saunders and Schoenly 1995; Hannington et al. 2016; Gartman et al. 2018; McLeish et al. 2021, 2024; Cano et al. 2023). Significantly, these processes could increase the Au content, greatly exceeding the maximum solubility of Au in the fluids under saturated conditions (e.g., Hannington et al. 2016), thereby facilitating the formation of high-grade gold ores. During fluid boiling and pyrite crystallization, gold is reduced from Au^+ to Au^0 due to the significant loss of sulfur. These processes can be represented by the following reaction:

$$\left[Au(HS)_2\right]^- + [HS]^- + Fe^{2+} = Au^0 + FeS_{2(S)} + H_2S_{(g)} + 1/2H_{2(g)}.$$

Subsequently, the physical effects of boiling further trigger the formation of gold colloids from gold monomers (Au^0) via nucleation and coarsening (Thanh et al. 2014; McLeish et al. 2021). The rapid crystallization of pyrite (Py1) could significantly deplete the Fe content in the fluids, particularly in the closed hydrothermal systems typical of quartz-vein gold deposits, where Fe is not replenished from wall rocks (Zhu et al. 2018). Consequently, crystallization of pyrite stopped once Fe concentrations dropped below saturation. During these short processes of pyrite crystallization, gold colloids, which were likely coated and charged by ligands of HS^- (Si et al. 2018), remained stably dispersed in the fluids. After that, boiling-related increases in pH (McLeish et al. 2021; Wang et al. 2022) could promote the precipitation of some minerals containing elements (e.g., Cu, Pb, and Zn) that were transported as chloride complexes in the ore fluids (Reed and Palandri 2006). The precipitation of these sulfides (minor in this stage) consumed the residual ligands of HS^-, thereby destabilizing the gold colloids. Given that the nanoparticle phase is generally short-lived (Thanh et al. 2014; McLeish et al. 2021; Petrella et al. 2022), the destabilized colloids rapidly aggregated to form coarse gold grains. Furthermore, boiling would enhance collisions between gold particles and pyrite crystals, as well as chalcopyrite, sphalerite and galena, leading to the encapsulation of visible gold along primary sub-grain boundaries of pyrite. These processes are illustrated in Fig. 11. Although direct evidence for gold nanoparticles or colloids is hardly preserved due to their instability, this alternative mechanism can best explain the high-grade visible gold occurring as intergranular particles in the primary pyrite aggregates. Notably, the LA-ICP-MS time-resolved depth profiles of Py1 exhibit signals indicative of Au–Ag inclusions, suggesting the presence of gold or electrum nanoparticles (Fig. 6c). This interpretation is further supported by the study of Yang et al. (2016) on the Jiaodong gold province, in which transmission electron microscopy (TEM) imaging also revealed the possible presence of gold nanoparticles within pyrite.

6 Conclusions

In situ textural and geochemical analyses of pyrite were conducted to decipher the specific processes controlling the formation of visible gold in the high-grade Linglong gold deposit of the Jiaodong gold province, leading to the following major conclusions:

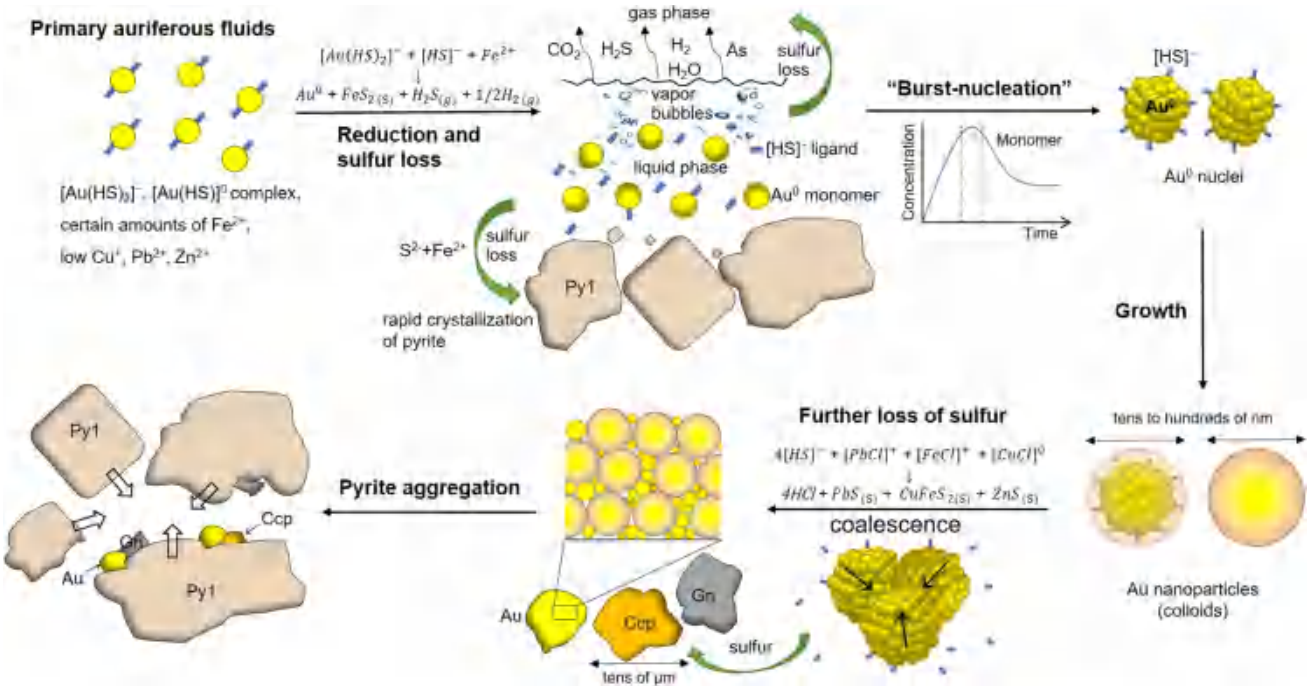

Fig. 11 Schematic illustration for a model of visible gold formation under fluid boiling at the Linglong gold deposit

1. Two main types of pyrite were identified in hydrothermal stages II (Py1) and III (Py2). Visible gold predominantly occurs as intergranular particles in Py1 aggregates that have lower concentrations of Au (mean: 0.032 ppm) with a narrow δ^{34}S range (4.86‰–6.75‰). Py2 has higher concentrations of Au (mean: 0.304 ppm) with progressively increasing δ^{34}S values (5.25‰–10.14‰) over time, but lacks visible gold mineralization.
2. The physicochemical conditions of the ore-forming fluids were unstable and characterized by disequilibrium during stage II, becoming more stable with near-equilibrium conditions during stage III.
3. Fluid boiling led to the unstable, disequilibrium physicochemical conditions and the efficient, rapid deposition of Au only during hydrothermal stage II. Gold colloids likely occurred briefly and promoted the formation of visible gold.

Acknowledgements We are grateful to Wei-Qing Sun for his help in field sampling and to Shao-Hua Dong, Zhi-Hui Dai, Xue Zhang, and Dan Chen for their help in analyses. We also extend our appreciation to the anonymous reviewers and editors for their constructive comments, which greatly contributed to the improvement of the manuscript. This study is financially supported by the National Natural Science Foundation of China (Grant Nos. 42302106 and 42102089), National Foundation for Guiding Local Science and Technology Development (Guizhou [2024] 043), and Innovation and Development Fund of Science and Technology of Institute of Geochemistry, Chinese Academy of Sciences (Grant No. 2025-1).

Author contributions Hong Wang: Investigation, Data curation, Formal analysis, Writing—original draft, Funding acquisition; Ting-Guang Lan: Investigation, Conceptualization, Supervision, Funding acquisition, Writing—review & editing; Lang-Ye Zhao: Investigation, Data curation; Hong-Rui Fan: Conceptualization; Zhan-Ping Li: Data curation; Huan-Long Hu: Investigation; Zi-Qi Xu: Data curation; Hong-Wei Peng: Funding acquisition; Lei Shu: Investigation.

Funding National Natural Science Foundation of China, 42302106, Hong Wang, 42102089, Hong-Wei Peng, National Foundation for Guiding Local Science and Technology Development, Guizhou [2024] 043, Tingguang Lan, Innovation and Development Fund of Science and Technology of Institute of Geochemistry, Chinese Academy of Sciences, 2025-1, Tingguang Lan

Declarations

Conflict of interest The authors declare that they have no known competing financial or non-financial conflict of interests that are directly or indirectly related to the work reported in this paper.

References

Bao ZA, Chen L, Zong CL, Yuan HL, Chen KY, Dai MN (2017) Development of pressed sulfide powder tablets for *in situ* sulfur and lead isotope measurement using LA-MC-ICP-MS. Int J Mass Spectrom 421:255–262. https://doi.org/10.1016/j.ijms.2017.07.015

Belousov I, Danyushevsky L, Goemann K, Gilbert S, Olin P, Thompson J, Lounejeva E, Garbe-Schönberg D (2023) STDGL3, a reference material for analysis of sulfide minerals by laser ablation ICP-MS: an assessment of matrix effects and the impact of laser wavelengths and pulse widths. Geostand Geoanal Res 47(3):493–508. https://doi.org/10.1111/ggr.12512

Cai Y-C, Fan H-R, Santosh M, Liu X, Hu F-F, Yang K-F, Lan T-G, Yang Y-H, Liu YS (2013) Evolution of the lithospheric mantle beneath the southeastern North China Craton: constraints from mafic dikes in the Jiaobei terrain. Gondwana Res 24(2):601–621. https://doi.org/10.1016/j.gr.2012.11.013

Cai Y-C, Fan H-R, Santosh M, Hu F-F, Yang K-F, Hu ZC (2015) Subduction-related metasomatism of the lithospheric mantle beneath the southeastern North China Craton: evidence from mafic to intermediate dykes in the northern Sulu orogen. Tectonophysics 659:137–151. https://doi.org/10.1016/j.tecto.2015.07.037

Cano N, González-Jiménez JM, Camprubí A, Domínguez-Carretero D, González-Partida E, Proenza JA (2023) Nanomaterial accumulation in boiling brines enhances epithermal bonanzas. Sci Rep 13:14985. https://doi.org/10.1038/s41598-023-41756-4

Chen L, Yuan HL, Chen KY, Bao ZA, Zhu LM, Liang P (2019) *In situ* sulfur isotope analysis by laser ablation MC-ICPMS and a case study of the Erlihe Zn-Pb ore deposit, Qinling orogenic belt, Central China. J Asian Earth Sci 176:325–336. https://doi.org/10.1016/j.jseaes.2019.02.017

Ciobanu CL, Cook NJ, Utsunomiya S, Kogagwa M, Green L, Gilbert S, Wade B (2012) Gold-telluride nanoparticles revealed in arsenic-free pyrite. Am Mineral 97(8–9):1515–1518. https://doi.org/10.2138/am.2012.4207

Cook NJ, Ciobanu CL, Mao JW (2009) Textural control on gold distribution in As-free pyrite from the Dongping, Huangtuliang and Hougou gold deposits, North China Craton (Hebei Province, China). Chem Geol 264(1–4):101–121. https://doi.org/10.1016/j.chemgeo.2009.02.020

Deditius AP, Reich M, Kesler SE, Utsunomiya S, Chryssoulis SL, Walshe J, Ewing RC (2014) The coupled geochemistry of Au and As in pyrite from hydrothermal ore deposits. Geochim Cosmochim Acta 140:644–670. https://doi.org/10.1016/j.gca.2014.05.045

Deng J, Liu XF, Wang QF, Dilek Y, Liang YY (2017) Isotopic characterization and petrogenetic modeling of Early Cretaceous mafic diking: lithospheric extension in the North China Craton, eastern Asia. GSA Bull 129(11–12):1379–1407. https://doi.org/10.1130/b31609.1

Deng J, Yang L-Q, Groves DI, Zhang L, Qiu K-F, Wang Q-F (2020) An integrated mineral system model for the gold deposits of the giant Jiaodong province, Eastern China. Earth Sci Rev 208:103274. https://doi.org/10.1016/j.earscirev.2020.103274

Falkenberg JJ, Keith M, Haase KM, Bach W, Klemd R, Strauss H, Yeo IA, Rubin KH, Storch B, Anderson MO (2021) Effects of fluid boiling on Au and volatile element enrichment in submarine arc-related hydrothermal systems. Geochim Cosmochim Acta 307:105–132. https://doi.org/10.1016/j.gca.2021.05.047

Fan HR, Hu FF, Yang JH, Zhai MG (2007) Fluid evolution and large-scale gold metallogeny during Mesozoic tectonic transition in the Jiaodong Peninsula, Eastern China. Geol Soc Lond Spec Publ 280(1):303–316. https://doi.org/10.1144/sp280.16

Feng K, Fan HR, Groves DI, Yang KF, Hu FF, Liu X, Cai YC (2020) Geochronological and sulfur isotopic evidence for the genesis of the post-magmatic, deeply sourced, and anomalously gold-rich Daliuhang orogenic deposit, Jiaodong, China. Miner Deposita 55(2):293–308. https://doi.org/10.1007/s00126-019-00882-8

Fougerouse D, Micklethwaite S, Tomkins AG, Mei Y, Kilburn M, Guagliardo P, Fisher LA, Halfpenny A, Gee M, Paterson D, Howard DL (2016a) Gold remobilisation and formation of high grade ore shoots driven by dissolution-reprecipitation replacement and Ni substitution into auriferous arsenopyrite. Geochim Cosmochim Acta 178:143–159. https://doi.org/10.1016/j.gca.2016.01.040

Fougerouse D, Reddy SM, Saxey DW, Rickard WDA, van Riessen A, Micklethwaite S (2016b) Nanoscale gold clusters in arsenopyrite controlled by growth rate not concentration: evidence from atom probe microscopy. Am Mineral 101(8):1916–1919. https://doi.org/10.2138/am-2016-5781ccbyncnd

Gartman A, Hannington M, Jamieson JW, Peterkin B, Garbe-Schönberg D, Findlay AJ, Fuchs S, Kwasnitschka T (2018) Boiling-induced formation of colloidal gold in black smoker hydrothermal fluids. Geology 46(1):39–42. https://doi.org/10.1130/g39492.1

Goldfarb RJ, Santosh M (2014) The dilemma of the Jiaodong gold deposits: are they unique? Geosci Front 5(2):139–153. https://doi.org/10.1016/j.gsf.2013.11.001

Goss SC, Wilde SA, Wu FY, Yang JH (2010) The age, isotopic signature and significance of the youngest Mesozoic granitoids in the Jiaodong Terrane, Shandong Province, North China Craton. Lithos 120(3–4):309–326. https://doi.org/10.1016/j.lithos.2010.08.019

Groves DI, Santosh M (2016) The giant Jiaodong gold province: the key to a unified model for orogenic gold deposits? Geosci Front 7(3):409–417. https://doi.org/10.1016/j.gsf.2015.08.002

Groves DI, Goldfarb RJ, Gebre-Mariam M, Hagemann SG, Robert F (1998) Orogenic gold deposits: a proposed classification in the context of their crustal distribution and relationship to other gold deposit types. Ore Geol Rev 13(1–5):7–27. https://doi.org/10.1016/s0169-1368(97)00012-7

Guo L-N, Goldfarb RJ, Wang Z-L, Li R-H, Chen B-H, Li J-L (2017) A comparison of Jiaojia- and Linglong-type gold deposit ore-forming fluids: do they differ? Ore Geol Rev 88:511–533. https://doi.org/10.1016/j.oregeorev.2016.12.003

Hannington M, Harðardóttir V, Garbe-Schönberg D, Brown KL (2016) Gold enrichment in active geothermal systems by accumulating colloidal suspensions. Nat Geosci 9(4):299–302. https://doi.org/10.1038/ngeo2661

Hastie ECG, Kontak DJ, Lafrance B (2020) Gold remobilization: insights from gold deposits in the Archean Swayze greenstone belt, Abitibi subprovince, Canada. Econ Geol 115(2):241–277. https://doi.org/10.5382/econgeo.4709

Hastie ECG, Schindler M, Kontak DJ, Lafrance B (2021) Transport and coarsening of gold nanoparticles in an orogenic deposit by dissolution–reprecipitation and ostwald ripening. Commun Earth Environ 2:57. https://doi.org/10.1038/s43247-021-00126-6

Hochella MF Jr, Lower SK, Maurice PA, Penn RL, Sahai NT, Sparks DL, Twining BS (2008) Nanominerals, mineral nanoparticles, and earth systems. Science 319(5870):1631–1635. https://doi.org/10.1126/science.1141134

Hou ML, Jiang YH, Jiang SY, Ling HF, Zhao KD (2007) Contrasting origins of late Mesozoic adakitic granitoids from the northwestern Jiaodong Peninsula, East China: implications for crustal thickening to delamination. Geol Mag 144(4):619–631. https://doi.org/10.1017/s0016756807003494

Jahn BM, Liu D, Wan Y, Song B, Wu J (2008) Archean crustal evolution of the Jiaodong Peninsula, China, as revealed by zircon SHRIMP geochronology, elemental and Nd-isotope geochemistry. Am J Sci 308(3):232–269. https://doi.org/10.2475/03.2008.03

Jian W, Mao JW, Lehmann B, Cook NJ, Xie GQ, Liu P, Duan C, Alles J, Niu ZJ (2021) Au-Ag-Te–rich melt inclusions in hydrothermal gold-quartz veins, Xiaoqinling lode gold district, Central China. Econ Geol 116(5):1239–1248. https://doi.org/10.5382/econgeo.4811

Jiang P, Yang KF, Fan HR, Liu X, Cai YC, Yang YH (2016) Titanite-scale insights into multi-stage magma mixing in early Cretaceous of NW Jiaodong terrane, North China craton. Lithos 258:197–214. https://doi.org/10.1016/j.lithos.2016.04.028

Kusebauch C, Gleeson SA, Oelze M (2019) Coupled partitioning of Au and as into pyrite controls formation of giant Au deposits. Sci Adv 5(5):eaav5891. https://doi.org/10.1126/sciadv.aav5891

Kutzschbach M, Dunkel F, Kusebauch C, Schiperski F, Börner F, Drake H, Klimm K, Keith M (2024) Arsenic-poor fluids promote strong As partitioning into pyrite. Geochim Cosmochim Acta 376:37–53. https://doi.org/10.1016/j.gca.2024.05.027

Lan T-G, Wang H, Fan H-R, Ulrich T, Hu H-L, Chen Y-W, Shu L (2023) Gold endowment and unloading along pathway for giant gold mineralization: insights from spatiotemporal variations of *in situ* pyrite geochemistry and gold fineness from the Jiaodong gold deposits, North China Craton. Gondwana Res 118:58–75. https://doi.org/10.1016/j.gr.2023.02.008

Li CF, Wang JL, Zhou ZY, Geng JH, Chen B, Yang FL, Wu JS, Yu P, Zhang XB, Zhang SW (2012) 3D geophysical characterization of the Sulu-Dabie orogen and its environs. Phys Earth Planet Inter 192–193:35–53. https://doi.org/10.1016/j.pepi.2012.01.003

Li XH, Fan HR, Yang KF, Hollings P, Liu X, Hu FF, Cai YC (2018) Pyrite textures and compositions from the Zhuangzi Au deposit, southeastern North China Craton: implication for ore-forming processes. Contrib Mineral Petrol 173(9):73. https://doi.org/10.1007/s00410-018-1501-2

Li Q, Song H, Chi GX, Zhang GY, Xu ZQ (2021) Genesis of visible gold in pyrite in the Zhaoxian gold deposit, Jiaodong gold province, China: constraints from EBSD micro-structural and LA-ICP-MS elemental analyses. Ore Geol Rev 139:104591. https://doi.org/10.1016/j.oregeorev.2021.104591

Liang YY, Liu XF, Qin C, Li Y, Chen J, Jiang JY (2017) Petrogenesis of early Cretaceous mafic dikes in southeastern Jiaolai basin, Jiaodong Peninsula, China. Int Geol Rev 59(2):131–150. https://doi.org/10.1080/00206814.2016.1213666

Liang Q-L, Xie ZJ, Song X-Y, Wirth R, Xia Y, Cline J (2021) Evolution of invisible Au in arsenian pyrite in carlin-type Au deposits. Econ Geol 116(2):515–526. https://doi.org/10.5382/econgeo.4781

Ling WL, Xie XJ, Liu XM, Cheng JP (2007) Zircon U-Pb dating on the Mesozoic volcanic suite from the Qingshan Group stratotype section in eastern Shandong Province and its tectonic significance. Sci China Ser D Earth Sci 50(6):813–824. https://doi.org/10.1007/s11430-007-2065-6

McLeish DF, Williams-Jones AE, Vasyukova OV, Clark JR, Board WS (2021) Colloidal transport and flocculation are the cause of the hyperenrichment of gold in nature. Proc Natl Acad Sci USA 118:2100689118. https://doi.org/10.1073/pnas.2100689118

McLeish DF, Williams-Jones AE, Clark JR, Stern RA (2024) Extreme shifts in pyrite sulfur isotope compositions reveal the path to bonanza gold. Proc Natl Acad Sci U S A 121:e2402116121

Mills SE, Tomkins AG, Weinberg RF, Fan H-R (2015) Implications of pyrite geochemistry for gold mineralisation and remobilisation in the Jiaodong gold district, Northeast China. Ore Geol Rev 71:150–168. https://doi.org/10.1016/j.oregeorev.2015.04.022

Paton C, Hellstrom J, Paul B, Woodhead J, Hergt J (2011) Iolite: freeware for the visualisation and processing of mass spectrometric data. J Anal at Spectrom 26(12):2508–2518. https://doi.org/10.1039/C1JA10172B

Peng HW, Fan HR, Liu X, Wen BJ, Zhang YW, Feng K (2021) New insights into the control of visible gold fineness and deposition: a case study of the Sanshandao gold deposit, Jiaodong, China. Am Mineral 106(1):135–149. https://doi.org/10.2138/am-2020-7475

Peterson EC, Mavrogenes JA (2014) Linking high-grade gold mineralization to earthquake-induced fault-valve processes in the Porgera gold deposit, Papua New Guinea. Geology 42(5):383–386. https://doi.org/10.1130/g35286.1

Petrella L, Thébaud N, Fougerouse D, Evans K, Quadir Z, Laflamme C (2020) Colloidal gold transport: a key to high-grade gold mineralization? Miner Deposita 55(7):1247–1254. https://doi.org/10.1007/s00126-020-00965-x

Petrella L, Thébaud N, Fougerouse D, Tattitch B, Martin L, Turner S, Suvorova A, Gain S (2022) Nanoparticle suspensions from carbon-rich fluid make high-grade gold deposits. Nat Commun 13:3795. https://doi.org/10.1038/s41467-022-31447-5

Pokrovski GS, Tagirov BR, Schott J, Hazemann JL, Proux O (2009) A new view on gold speciation in sulfur-bearing hydrothermal fluids from *in situ* X-ray absorption spectroscopy and quantum-chemical modeling. Geochim Cosmochim Acta 73(18):5406–5427. https://doi.org/10.1016/j.gca.2009.06.007

Pokrovski GS, Escoda C, Blanchard M, Testemale D, Hazemann JL, Gouy S, Kokh MA, Boiron MC, de Parseval F, Aigouy T, Menjot L, de Parseval P, Proux O, Rovezzi M, Béziat D, Salvi S, Kouzmanov K, Bartsch T, Pöttgen R, Doert T (2021) An arsenic-driven pump for invisible gold in hydrothermal systems. Geochem Persp Let 17:39–44. https://doi.org/10.7185/geochemlet.2112

Qiu YM, Groves DI, McNaughton NJ, Wang LG, Zhou TH (2002) Nature, age, and tectonic setting of granitoid-hosted, orogenic gold deposits of the Jiaodong Peninsula, eastern North China Craton, China. Miner Deposita 37(3):283–305. https://doi.org/10.1007/s00126-001-0238-3

Rauchenstein-Martinek K, Wagner T, Wälle M, Heinrich CA (2014) Gold concentrations in metamorphic fluids: a LA-ICPMS study of fluid inclusions from the Alpine orogenic belt. Chem Geol 385:70–83. https://doi.org/10.1016/j.chemgeo.2014.07.018

Reed MH (2006) Sulfide mineral precipitation from hydrothermal fluids. Rev Mineral Geochem 61(1):609–631. https://doi.org/10.2138/rmg.2006.61.11

Reich M, Kesler SE, Utsunomiya S, Palenik CS, Chryssoulis SL, Ewing RC (2005) Solubility of gold in arsenian pyrite. Geochim Cosmochim Acta 69(11):2781–2796. https://doi.org/10.1016/j.gca.2005.01.011

Román N, Reich M, Leisen M, Morata D, Barra F, Deditius AP (2019) Geochemical and micro-textural fingerprints of boiling in pyrite. Geochim Cosmochim Acta 246:60–85. https://doi.org/10.1016/j.gca.2018.11.034

Saunders J, Burke M (2017) Formation and aggregation of gold (electrum) nanoparticles in epithermal ores. Minerals 7(9):163. https://doi.org/10.3390/min7090163

Saunders JA, Schoenly PA (1995) Boiling, colloid nucleation and aggregation, and the genesis of bonanza Au-Ag ores of the sleeper deposit, Nevada. Miner Deposita 30(3):199–210. https://doi.org/10.1007/BF00196356

Saunders JA, Burke M, Brueseke ME (2020) Scanning-electron-microscope imaging of gold (electrum) nanoparticles in middle Miocene bonanza epithermal ores from northern Nevada, USA. Miner Deposita 55(3):389–398. https://doi.org/10.1007/s00126-019-00935-y

Shields SP, Richards VN, Buhro WE (2010) Nucleation control of size and dispersity in aggregative nanoparticle growth. A study of the coarsening kinetics of thiolate-capped gold nanocrystals. Chem Mater 22(10):3212–3225. https://doi.org/10.1021/cm100458b

Si KJ, Chen Y, Shi QQ, Cheng WL (2018) Nanoparticle superlattices: the roles of soft ligands. Adv Sci 5:1700179. https://doi.org/10.1002/advs.201700179

Simmons SF, Brown KL (2006) Gold in magmatic hydrothermal solutions and the rapid formation of a giant ore deposit. Science 314(5797):288–291. https://doi.org/10.1126/science.1132866

Song M-C, Li S-Z, Santosh M, Zhao SJ, Yu S, Yi P-H, Cui S-X, Lv G-X, Xu J-X, Song Y-X, Zhou M-L (2015) Types, characteristics and metallogenesis of gold deposits in the Jiaodong Peninsula, Eastern North China Craton. Ore Geol Rev 65:612–625. https://doi.org/10.1016/j.oregeorev.2014.06.019

Sung YH, Brugger J, Ciobanu CL, Pring A, Skinner W, Nugus M (2009) Invisible gold in arsenian pyrite and arsenopyrite from a multistage Archaean gold deposit: Sunrise Dam,

Eastern Goldfields Province, Western Australia. Miner Deposita 44(7):765–791. https://doi.org/10.1007/s00126-009-0244-4

Syverson DD, Ono S, Shanks WC, Seyfried WE Jr (2015) Multiple sulfur isotope fractionation and mass transfer processes during pyrite precipitation and recrystallization: an experimental study at 300 and 350 ℃. Geochim Cosmochim Acta 165:418–434. https://doi.org/10.1016/j.gca.2015.06.022

Tardani D, Reich M, Deditius AP, Chryssoulis S, Sánchez-Alfaro P, Wrage J, Roberts MP (2017) Copper–arsenic decoupling in an active geothermal system: a link between pyrite and fluid composition. Geochim Cosmochim Acta 204:179–204. https://doi.org/10.1016/j.gca.2017.01.044

Tauson VL, Kravtsova RG, Smagunov NV, Spiridonov AM, Grebenshchikova VI, Budyak AE (2014) Structurally and superficially bound gold in pyrite from deposits of different genetic types. Russ Geol Geophys 55(2):273–289. https://doi.org/10.1016/j.rgg.2014.01.011

Thanh NTK, MacLean N, Mahiddine S (2014) Mechanisms of nucleation and growth of nanoparticles in solution. Chem Rev 114(15):7610–7630. https://doi.org/10.1021/cr400544s

Ulrich T, Long DGF, Kamber BS, Whitehouse MJ (2011) *In situ* trace element and sulfur isotope analysis of pyrite in a Paleoproterozoic gold placer deposit, Pardo and Clement townships, Ontario, Canada. Econ Geol 106(4):667–686. https://doi.org/10.2113/econgeo.106.4.667

Wagner T, Fusswinkel T, Wälle M, Heinrich CA (2016) Microanalysis of fluid inclusions in crustal hydrothermal systems using laser ablation methods. Elements 12(5):323–328. https://doi.org/10.2113/gselements.12.5.323

Wan YS, Song B, Liu DY, Wilde SA, Wu JS, Shi YR, Yin XY, Zhou HY (2006) Shrimp U-Pb zircon geochronology of Palaeoproterozoic metasedimentary rocks in the North China Craton: evidence for a major Late Palaeoproterozoic tectonothermal event. Precambr Res 149(3–4):249–271. https://doi.org/10.1016/j.precamres.2006.06.006

Wang H, Lan TG, Fan HR, Huang ZL, Hu HL, Chen YH, Tang YW, Li J (2022) Fluid origin and critical ore-forming processes for the giant gold mineralization in the Jiaodong Peninsula, China: constraints from *in situ* elemental and oxygen isotopic compositions of quartz and LA–ICP–MS analysis of fluid inclusions. Chem Geol 608:121027. https://doi.org/10.1016/j.chemgeo.2022.121027

Wang H, Lan TG, Fan HR, Zhao LY, Hu HL, Peng HW, Xu Y, Shu L, Dai ZH (2024) Anomalous cobalt enrichment in pyrite from an altered mafic dike in the Linglong gold deposit, Jiaodong Peninsula, China: mechanisms and implications. Ore Geol Rev 170:106139. https://doi.org/10.1016/j.oregeorev.2024.106139

Wen B-J, Fan H-R, Santosh M, Hu F-F, Pirajno F, Yang K-F (2015) Genesis of two different types of gold mineralization in the Linglong gold field, China: constrains from geology, fluid inclusions and stable isotope. Ore Geol Rev 65:643–658. https://doi.org/10.1016/j.oregeorev.2014.03.018

Wen BJ, Fan HR, Hu FF, Liu X, Yang KF, Sun ZF, Sun ZF (2016) Fluid evolution and ore genesis of the giant Sanshandao gold deposit, Jiaodong gold province, China: constrains from geology, fluid inclusions and H-O–S–He–Ar isotopic compositions. J Geochem Explor 171:96–112. https://doi.org/10.1016/j.gexplo.2016.01.007

White NC, Hedenquist JW (1995) Epithermal gold deposits: Styles. Charact Expl SEG Discov 23:1–13. https://doi.org/10.5382/segnews.1995-23.fea

Williams-Jones AE, Bowell RJ, Migdisov AA (2009) Gold in solution. Elements 5(5):281–287. https://doi.org/10.2113/gselements.5.5.281

Wilson SA, Ridley WI, Koenig AE (2002) Development of sulfide calibration standards for the laser ablation inductively-coupled plasma mass spectrometry technique. J Anal at Spectrom 17(4):406–409. https://doi.org/10.1039/b108787h

Wu YB, Zheng YF (2013) Tectonic evolution of a composite collision orogen: an overview on the Qinling–Tongbai–Hong'an–Dabie–Sulu orogenic belt in Central China. Gondwana Res 23(4):1402–1428. https://doi.org/10.1016/j.gr.2012.09.007

Xian HY, He HP, Zhu JX, Qiu KF, Li Y, Yang YP, Xing JQ, Tan W, Tsuchiyama A, Yastake M, Enju S, Miyake A, Zhu RL (2022) Hyperenrichment of gold in pyrite induced by solid-state transportation. Commun Earth Environ 3:308. https://doi.org/10.1038/s43247-022-00628-x

Xing YL, Brugger J, Tomkins A, Shvarov Y (2019) Arsenic evolution as a tool for understanding formation of pyritic gold ores. Geology 47(4):335–338. https://doi.org/10.1130/g45708.1

Xue SM, Liang YY, Shu L, Xue WH, Zhang CX, Shen CH, He B, Wang HY, Fang YY (2025) Genesis of the Jiuqu gold deposit, Jiaodong gold province, China: constraints on the texture, mineral geochemistry, and sulfur isotope of pyrite. Acta Geochim 44(3):631–647. https://doi.org/10.1007/s11631-024-00747-6

Yang JH, Zhou XH (2001) Rb-Sr, Sm-Nd, and Pb isotope systematics of pyrite: implications for the age and genesis of lode gold deposits. Geology 29(8):711. https://doi.org/10.1130/0091-7613(2001)029%3c0711:rssnap%3e2.0.co;2

Yang K-F, Fan H-R, Santosh M, Hu F-F, Wilde SA, Lan T-G, Lu L-N, Liu Y-S (2012) Reactivation of the Archean lower crust: implications for zircon geochronology, elemental and Sr–Nd–Hf isotopic geochemistry of late Mesozoic granitoids from northwestern Jiaodong Terrane, the North China Craton. Lithos 146–147:112–127. https://doi.org/10.1016/j.lithos.2012.04.035

Yang L-Q, Deng J, Wang Z-L, Guo L-N, Li R-H, Groves DI, Danyushevsky LV, Zhang C, Zheng X-L, Zhao H (2016) Relationships between gold and pyrite at the Xincheng gold deposit, Jiaodong Peninsula, China: implications for gold source and deposition in a brittle epizonal environment. Econ Geol 111(1):105–126. https://doi.org/10.2113/econgeo.111.1.105

Yuan ZZ, Li ZK, Li JW, Zhao XF, Wu YF, Xu HJ, Sun HS (2021) Occurrence and remobilization of gold in the Dayingezhuang deposit in Jiaodong, North China Craton: evidence from textural and geochemical features of pyrite. Ore Geol Rev 136:104243. https://doi.org/10.1016/j.oregeorev.2021.104243

Zhang L, Weinberg RF, Yang L-Q, Groves DI, Sai S-X, Matchan E, Phillips D, Kohn BP, Miggins DP, Liu Y, Deng J (2020) Mesozoic orogenic gold mineralization in the Jiaodong Peninsula, China: a focused event at 120 ± 2 Ma during cooling of pregold granite intrusions. Econ Geol 115(2):415–441. https://doi.org/10.5382/econgeo.4716

Zheng YF, Zhao ZF, Chen RX (2019) Ultrahigh-pressure metamorphic rocks in the Dabie–Sulu orogenic belt: compositional inheritance and metamorphic modification. In (eds. Zhang L, Zhang Z, Schertl H-P, Wei C) HP–UHP Metamorphism and Tectonic Evolution of Orogenic Belts. Geol Soc Lond Spec Publ 474(1):89–132. https://doi.org/10.1144/sp474.9

Zhou HY, Wirth R, Gleeson SA, Schreiber A, Mayanna S (2021) Three-dimensional and microstructural fingerprinting of gold nanoparticles at fluid-mineral interfaces. Am Mineral 106(1):97–104. https://doi.org/10.2138/am-2021-7696

Zhu Z-Y, Jiang S-Y, Mathur R, Cook NJ, Yang T, Wang M, Ma L, Ciobanu CL (2018) Iron isotope behavior during fluid/rock interaction in K-feldspar alteration zone–a model for pyrite in gold deposits from the Jiaodong Peninsula, East China. Geochim Cosmochim Acta 222:94–116. https://doi.org/10.1016/j.gca.2017.10.001